ORCA – Online Research @ Cardiff

Forcefield Evaluation and Accelerated Molecular Dynamics Simulation of Zn(II) Binding to N-Terminus of Amyloid-β

Nadiyah Al-Shammari, Loizos Savva, Oliver Kennedy-Britten, James A. Platts*

School of Chemistry, Cardiff University, Park Place, Cardiff CF10 3AT, UK.

* Author for correspondence. Email: platts@cardiff.ac.uk   Phone: +44-2920-874950

Abstract

We report conventional and accelerated molecular dynamics simulation of Zn(II) bound to the N-terminus of amyloid-β. By comparison against NMR data for the experimentally determined binding mode, we find that certain combinations of forcefield and solvent model perform acceptably in describing the size, shape and secondary structure, and that there is no appreciable difference between implicit and explicit solvent models. We therefore used the combination of ff14SB forcefield and GBSA solvent model to compare the result of different binding modes of Zn(II) to the same peptide, using accelerated MD to enhance sampling and comparing the free peptide simulated in the same way. We show that Zn(II) imparts significant rigidity to the peptide, disrupts the secondary structure and pattern of salt bridges seen in the free peptide, and induces closer contact between residues. Free energy surfaces in 1 or 2 dimensions further highlight the effect of metal coordination on peptide's spatial extent. We also provide evidence that accelerated MD provides improved sampling over conventional MD by visiting as many or more configurations in much shorter simulation times.

Keywords

Amyloid-β, Molecular dynamics, Forcefield, Zinc, Free energy

Highlights

- AMBER forcefield reproduces NMR structure of Zn(II) bound to N-terminal fragment of Aβ.
- Implicit solvent performs at least as well as explicit in this regard.
- Accelerated MD shows subtle difference in structure and dynamics for different binding modes.
- Free energy surface shows restriction in size and flexibility due to Zn-binding.

Introduction

Alzheimer's disease is one of the greatest challenges facing 21st century healthcare.[1] Its aetiology is complex and not fully understood, but the importance of the amyloid-β (Aβ) peptide seems clear. This peptide, typically 40 or 42 amino acids in length, is observed to aggregate into fibrils in diseased brains but is also present in healthy patients, such that the trigger for aggregation is one focus of research into disease onset.[2–4] Environmental factors such as age, diet and smoking have all been implicated, along with inflammation due to reactive oxygen species (ROS).[5] One hypothesis on disease onset involves the role of transition metals, most notably copper, zinc and iron:[6–8] age and environment can affect the tightly controlled homeostasis of these metals. All three ions are known to bind to Aβ through the N-terminal sequence (residues 1 to 16) and affect the structure and dynamics of the peptide, which may in turn affect aggregation properties.[9–15] Moreover, the redox activity of Cu and Fe is a possible source of ROS.[16,17,26,18–25]

Numerous experimental techniques, including scattering and diffraction, magnetic resonance, circular dichroism, etc have shown in detail the sites and specificities of metal binding and its effect on peptide structure and dynamics.[13,27–30] Different models of transition metal ions of Zn, Cu, and Fe coordination have been proposed, with review articles summarising them.[31,32] The most important metal-binding sites for Zn(II) are the imidazoles of His6, His13 and His14 and the carboxylate of Glu11, with minor contributions from Asp1 and Glu3. It has also been stated that the peptide aggregates through intermolecular His-Zn-His bridges. Zirah et al used NMR to show that Zn(II) binds to Aβ (1-16) through N_δ of His6 and His14, N_ϵ of His13, and Glu11 carboxylate.[15] Another NMR study, this time in water-micelle solution, also showed that N_δ of His6 & His13 and His14 N_ϵ are involved in Zn(II) interaction to human Aβ (1-28), along with Asp1 amine, and/or Glu-11 COO^-.[33]

Simulation has emerged as a valuable complement to experiment in this field, offering the ability to monitor metals and their effects at atomic resolution.[34,35] Calculations based on quantum mechanics (QM), molecular mechanics (MM) as well as hybrid QM/MM methods have been applied to this problem.[36–41] However, there are significant challenges to suitable simulation of such systems: the complex electronic structure of transition metals is typically treated with QM methods, especially density functional theory, whereas the flexible nature of Aβ requires extensive sampling over the conformational space of the peptide. Recent work has shown how the accuracy of DFT can be built into more efficient MM approaches by extracting key parameters from suitable QM calculations.[40,42,43] However, there is significant debate in literature on the choice of MM forcefield for flexible peptides such as Aβ, as many parameter sets that are popular for biomolecular

simulation have been shown to be imbalanced in favour of more compact, folded structures.[44–46] Here, we have selected the experimental NMR study of Zirah et al to assess the suitability of simulation protocols, forcefields and solvent models for the specific problem of metal-Aβ interaction.

In addition, solvation is a key aspect of both coordination chemistry and biomolecular structure: many simulations of biomolecules employ explicit solvents,[47,48] while suitably chosen implicit models can offer improved sampling of conformational space but may favour compact conformations for flexible peptides.[49–51] In such cases, sampling is another vital aspect of simulations: even with the speed of MM in implicit solvent, molecular dynamics can struggle to visit all the conformations available to a peptide such as Aβ.[52] Enhanced sampling methods such as metadynamics or steered MD can be used to push simulations along a particular coordinate of interest.[53–56] Accelerated molecular dynamics (aMD) can achieve similar goals, but does so without requiring any pre-defined coordinate; instead, it adds a boost potential to prevent simulations becoming stuck in local energy minima.[57] Manipulation of variables permits the bias of sampling during the simulations. This is often done through the addition of a positive boost potential, for when the system's potential is lower than an energy barrier.[57] The disruption of the energy minima below the boost energy, allows the sampling of trajectories that would otherwise remain unexplored.[58] The free energy profile of the system and the average NVT ensemble are retrieved after the simulations have been completed using reweighting. The Boltzmann distribution of the boost energy permits the estimation of the ensemble average, while reweighting of the boost energy allows calculation of potential of mean forces, as explained by Miao et al.[57]

In this work, we use conventional and accelerated MD to simulate the N-terminal Aβ(1-16) sequence bound to divalent Zn(II) to probe the effect of metal coordination on structure and dynamics. This allows us to test a range of simulation protocols against experiment, to compare the effects of different Zn binding modes, and to compare the sampling obtained from aMD against previously reported conventional MD.

Computational Methods

All simulations were performed within the AMBER16 package.[59] Parameters suitable for AMBER-style forcefields were calculated using the metal centre parameter builder (MCPB.py) package[60] from B3LYP/6-31G(d)[61] data generated using Gaussian09.[62] Harmonic force constants compatible with AMBER simulation for metal-bound residues were extracted from DFT optimisation/frequency data via the Seminario[63] method, and atomic charges from DFT electrostatic potential using the restrained electrostatic potential (RESP)[64–66] fitting scheme. These were integrated with parameters from ff99SBildn, ff14SB, ff14SBonlysc and fb15 forcefields[67–69] using the LEaP utility.[70] Explicit solvent, in the form of TIP3P,[71] TIP4P[72] and FB[73] models, was added using LEaP and charge neutrality enforced by replacement of random waters with Na^+ or Cl^- ions as appropriate. Implicit solvent was simulated using the generalised Born surface area (GBSA) method,[74–76] with both default (igb=1) and modified (igb=8) parameterisations tested.

Tests of forcefield and solvent model were carried out using the NMR study of Zn(II) bound to the 16 N-terminal residues of Aβ (PDB entry 1ZE9),[15] for which 20 individual structures were reported. Experimental data was taken as mean/sd of these 20 structures, calculated using cpptraj.[77] Parameters were calculated for, and simulations started from, model 1 as reported in the PDB entry without any further modification. For comparison of binding modes, and with the metal-free peptide, the N-terminal Aβ sequence was built in MOE[78] in fully extended form, amidated at C-terminus but with N-terminus uncapped and so available for metal coordination. We then added Zn(II) ions following literature proposals,[33,79,80] as summarized by Nasica-Labouze et al.[32] The resulting structures minimised using the ligand field molecular mechanics (LFMM) approach set out by Deeth et al.[81] These minimised structures were best described as random coil, which was then used to generate parameters using the MCPB/LEaP procedure outlined above.

Conventional molecular dynamics (cMD) were carried out after minimisation in the chosen combination of forcefield and solvent model. These used the NVT ensemble at 310 K, with the Langevin thermostat,[82] with a timestep of 2 fs made possible by the use of SHAKE[83] restraints. For comparison of simulation with experiment, conventional MD simulation of three individual runs of 250 ns were employed. Parameters for the boost potential were taken from 250 ns of conventional MD. Once these parameters were established, three independent 250 ns aMD simulations were carried out and the first 50 ns discarded, resulting in 600 ns of aMD data six different binding modes and the free peptide. Figure S2 in Supporting Information shows evidence for 50 ns equilibration being suitable. Analysis of root mean square deviation (RMSD), root mean square fluctuation

(RMSF), the radius of gyration (Rg), secondary structure, backbone dihedrals, salt bridges, residue contacts, and free energy landscapes from this data were used to investigate the effects of metal binding on structure and flexibility of Aβ.

Results and Discussion

We start by examining the performance of different forcefields and solvent models in reproducing key structural features of the Zn(II) complex with Aβ1-16, using the 20 NMR structures from PDB entry 1ZE9 as a reference. The mean Rg from these structures is 7.42 Å with a standard deviation of 0.18 Å. Conventional MD was performed for 3 x 250 ns for multiple combinations of forcefield and solvent model: plots of RMSD relative to the experimental structure are shown in Supporting Information, showing the simulations are stable over this timescale.

Table 1 shows that most forcefields result in mean Rg within 1 standard deviation of the experimental value when combined with the GBSA implicit solvent model. The exception is ff14SBonlySC with the igb=8 solvent model, for which a significantly greater average is found. The standard deviation of Rg within implicit solvent is generally rather small, although it is apparent that most simulations visit both larger and smaller conformations than the experimental ensemble. We also report globularity from the diagonalized Rg tensor, giving a measure of the shape of the complex. The experimental average over 20 structures is 0.24 with sd of 0.04, indicating an elongated, prolate shape. Most implicit solvent simulations broadly reproduce this shape, falling within one sd of the experimental value. However, these promising mean values encompass significant ranges: ff14SB for instance visits conformations with globularity as low as 0.09 and as high as 0.78.

Table 1 Comparison of the radius of gyration and derived properties (Å).

		Mean	sd	Max	Min	Glob [a]
Experiment		**7.42**	**0.18**	**7.74**	**7.11**	**0.238**
ff14SB	igb=1	7.58	0.24	9.05	6.78	0.272
ff99SBildn	igb=1	7.66	0.42	9.93	6.64	0.267
ff14SBonlySC	igb=1	7.62	0.42	10.09	6.66	0.272
ff14SBonlySC	igb=8	8.42	0.37	10.36	7.04	0.203
fb15	igb=1	7.54	0.32	9.95	6.95	0.259
ff14SB	TIP3P	7.73	0.41	10.14	6.85	0.267
ff14SB	TIP4P	7.95	0.38	9.58	7.10	0.228
ff99SBildn	TIP3P	8.22	0.63	10.47	6.74	0.261
ff99SBildn	TIP4P	8.31	0.68	10.55	6.95	0.248
fb15	TIP3P	7.94	0.68	10.40	6.63	0.293
fb15	TIP3P-fb	7.88	0.54	10.42	6.83	0.279

[a] Globularity, defined as the ratio of smallest to the largest eigenvalue of Rg tensor

Explicit solvent simulations give rise to greater Rg for all combinations tested: ff14SB with TIP3P gives similar mean Rg, but notably larger sd and maximum, compared to implicit solvent. Changing to TIP4P increases mean Rg slightly, but reduces sd and maximum value, indicating that a less varied set of larger conformations is sampled with this model. In contrast, both ff99SBildn and fb15 give rise to much larger mean Rg with greater sd and maximum value, the latter in particular exhibiting values almost 3 Å larger than any observed in the experimental ensemble. All explicit solvent methods give globularity that is in good agreement with experiment, albeit with even greater ranges than for implicit models: fb15/TIP3P, for instance, has sd = 0.13 and visits conformations with globularity between 0.07 and 0.84.

Table 2 reports the overall secondary structure of experimental and simulated structures, with parallel/anti-parallel β-sheet, α/π/3_{10}-helix, and turn/bend/coil grouped into broader classes. A full breakdown of each secondary structure type can be found in Supporting Information. NMR finds no β-sheet character whatsoever, whereas all simulations give rise to a small amount of this structural

type. On average, one third of residues are found in helical form within the experimental ensemble: this is mostly in the form of 3_{10}-helices in residues 8 to 15. All implicit solvent models result in significant amounts of helix, with ff14SB and ff14SBonlySC/igb8 approaching the amount seen in experiment. Closer inspection (Figure 1) indicates that these simulations vary in the type and position of helical elements: both result in more α- but less 3_{10}-helix character than experiment, and in more helix formation closer to the N-terminal end of the peptide. Explicit solvent models significantly reduce the prevalence of helical character: ff14SB with either TIP3P/TIP4P maintain some of this form, but fb15 and especially ff99SBildn reduce it markedly.

Table 2 Comparison of overall secondary structure (%).

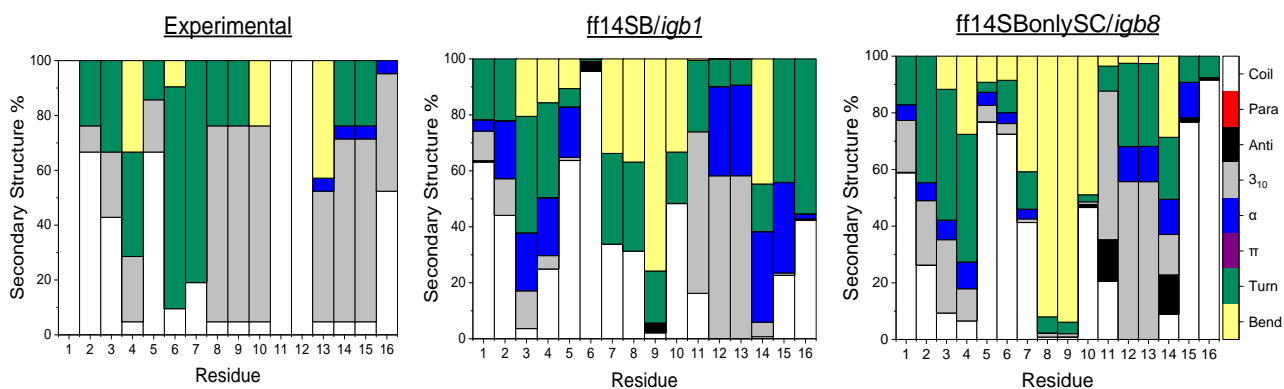|		Sheet	Helix	Other
Experiment		**0.0**	**33.3**	**66.7**
ff14SB	igb=1	0.5	27.4	72.1
ff99SBildn	igb=1	1.6	16.1	82.3
ff14SBonlySC	igb=1	3.4	19.7	76.9
ff14SBonlySC	igb=8	2.0	22.6	75.4
fb15	igb=1	1.5	19.5	79.0
ff14SB	TIP3P	0.9	20.5	78.6
ff14SB	TIP4P	0.3	23.4	76.3
ff99SBildn	TIP3P	3.7	8.4	87.9
ff99SBildn	TIP4P	3.9	6.1	90.1
fb15	TIP3P	4.2	8.2	87.6
fb15	TIP3P-fb	2.3	15.9	81.8

Figure 1 Secondary structure by residue for selected implicit solvent models.

Salt bridges are a key driver of peptide secondary structure in Aβ, with eight possible interactions within the N-terminal region. Of these, only four have significant occupation within the ensemble of NMR structures, although none are present in more than 50% of structures (Table 3). Comparison with MD data shows that no combination of forcefield and solvent model successfully captures this pattern of salt bridges. Most implicit solvent models lead to overestimation of Asp1-Arg5 occupancy and underestimation of Arg5-Asp7, while none represent the 50% occupancy of Glu3-Lys16. ff14SBonlySC is strongly dependent on the solvent model: with the default GBSA options, we find significant occupancy of Glu3-Arg5, whereas with the igb=8 settings, most salt bridges are much reduced. Explicit solvent models perform rather better in this regard, although again no single combination tested performs well for all four contacts, while Glu3-Lys16 is still under-represented by all. The combination of ff99SBildn with TIP3P solvent performs reasonably well in most cases, whereas in general the use of TIP4P and TIP3P-fb leads to diminished performance.

Table 3 Comparison of salt bridge occupancy (%).

		Asp1-Arg5	Glu3-Arg5	Arg5-Asp7	Glu3-Lys16
Experiment		**45**	**10**	**35**	**50**
ff14SB	igb=1	72	49	1	18
ff99SBildn	igb=1	55	16	29	9
ff14SBonlySC	igb=1	52	23	56	16
ff14SBonlySC	igb=8	14	3	20	2
fb15	igb=1	29	56	4	33
ff14SB	TIP3P	52	7	1	10
ff14SB	TIP4P	35	0	29	3
ff99SBildn	TIP3P	31	9	52	5
ff99SBildn	TIP4P	13	21	35	2
fb15	TIP3P	25	13	47	2
fb15	TIP3P-fb	15	33	1	4

Other properties considered, including Ramachandran maps of backbone dihedrals and prevalence of hydrogen bonds, did not show significant differences between forcefields and solvent models, and so are reported in Supporting Information and not discussed in detail. We conclude that none of the models perform perfectly for all properties and that there is no clear advantage in using explicit solvent over implicit models. Our main interest is in the changes in size and secondary structure induced by metal coordination, and so we have chosen ff14SB with default GBSA implicit solvent for further study.

Accelerated MD simulations were carried out using ff14SB/GBSA for the metal-free Aβ$_{1-16}$ and six complexes with Zn(II) bound through different residues/atoms. Three separate 250 ns simulations were combined into a single 600 ns trajectory by discarding the first 50ns of each run (data from separate runs are in Supporting Information). Figure 2 and Table 4 shows the proposed binding modes described in methodology and taken from literature,[6,15,32,33,38,79,80,84,85] with binding mode number 6 representing that seen in experiment.
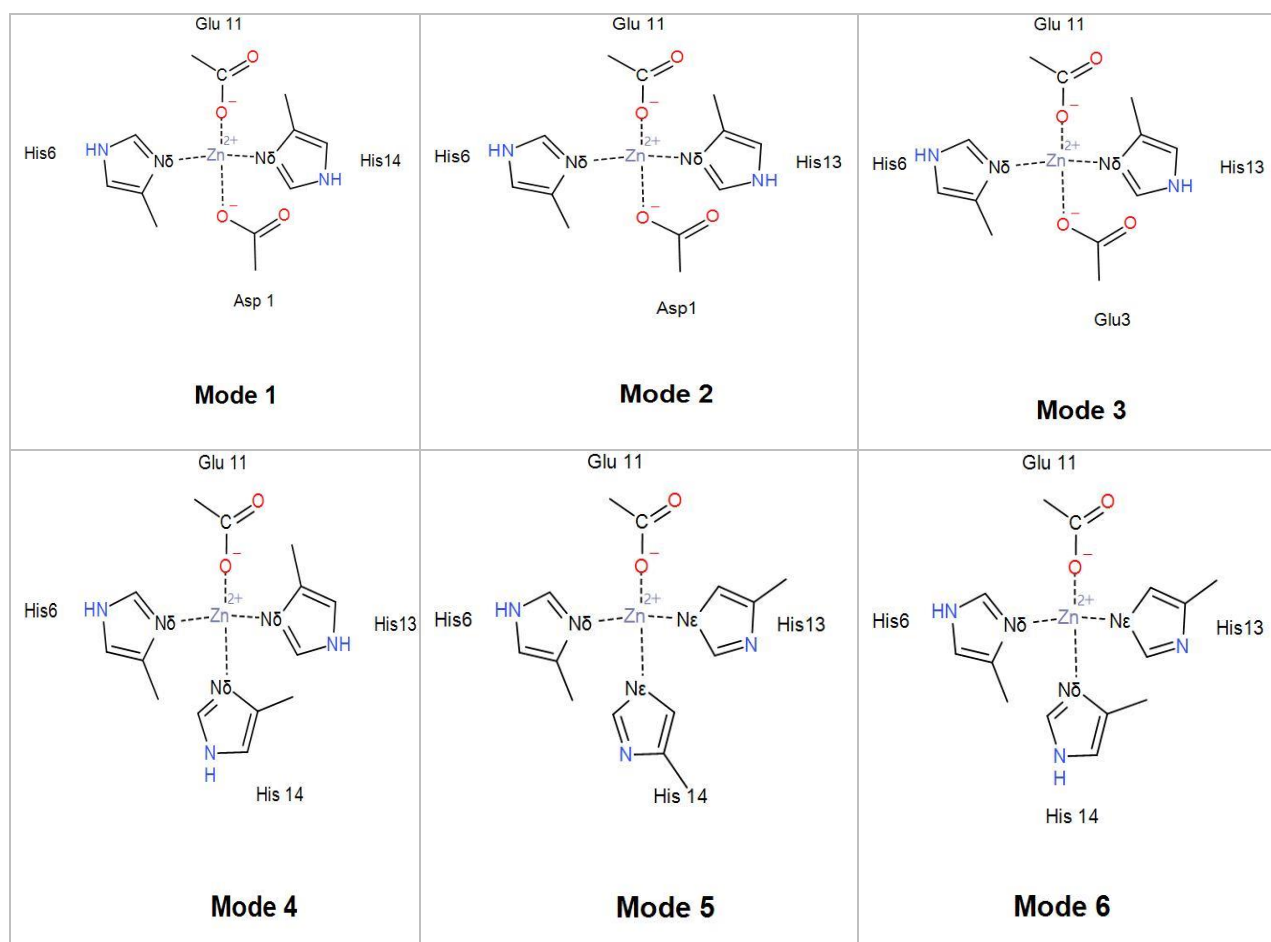
Figure 2 Different proposed binding modes of Aβ(1-16)binding to Zn(II)

Table 4 Different proposed binding modes of Aβ(1-16)binding to Zn(II)

	Coordination
Mode 1	His6 Nδ, His14 Nδ, Asp1 CO, Glu11 Oε
Mode 2	His6 Nδ, His13 Nδ, Asp1 CO, Glu11 Oε
Mode 3	His6 Nδ, His13 Nδ, Glu3 Oε, Glu11 Oε
Mode 4	His6 Nδ, His13 Nδ, His14 Nδ, Glu11 Oε
Mode 5	His6 Nδ, His13 Nε, His14 Nε, Glu11 Oε
Mode 6	His6 Nδ, His13 Nε, His14 Nδ, Glu11 Oε

Overall structural changes over simulation time are quantified using RMSD for stability measuring and Rg (Figure 3 and Table 5). Backbone RMSD relative to an initial minimized structure over a combined 600 ns of aMD simulation indicates that the free peptide explored more diverse and extended conformations than peptides bound to Zn, which remain more constrained and compact.

Mean RMSD of Aβ16 of 10.6 Å, with sd = 1.6 Å, is notably larger than for any Zn(II)-Aβ16 binding modes. Closer inspection shows that the free peptide undergoes larger and more frequent transitions in RMSD, ranging between *ca.* 5 and 15 Å, whereas Zn(II)-Aβ exhibits smaller and less frequent changes in RMSD ranged between 2.5 and 5.7 Å. Among all modes, Mode 1 shows the lowest RMSD values (Ave 2.65, Sd 0.37, and Max 4.63), whereas Mode 6 illustrates the highest average value.
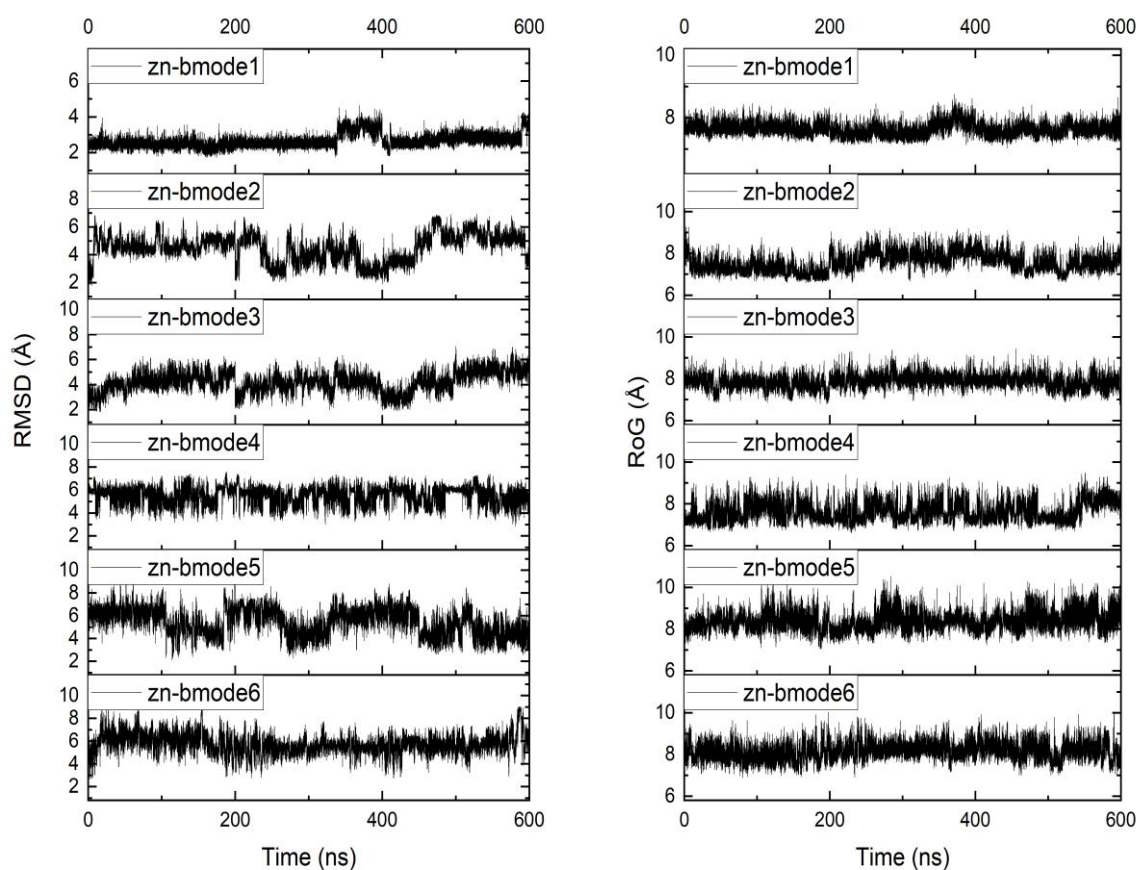

Figure 3 Backbone RMSD and Rg values of Zn(II)- and free Aβ-16. 600 ns of aMD data is reported, made up of the final 200 ns from each of three independent simulations each with different initial velocities.

Table 5 Backbone RMSD and Rg of free Aβ-16 and Zn^{2+}, (Å).

	RMSD				Rg			
	Mean	sd	Min	Max	Mean	sd	Min	Max
Zn(II)-Aβ16								
Mode 1	2.65	0.37	1.71	4.63	7.63	0.20	7.03	8.75
Mode 2	4.48	0.97	1.78	6.95	7.56	0.44	6.57	9.27
Mode 3	4.21	0.79	1.82	7.06	7.86	0.32	6.76	9.44
Mode 4	5.52	0.70	2.84	7.59	7.62	0.44	6.60	9.51
Mode 5	5.48	1.16	2.11	9.05	8.37	0.43	7.04	10.97
Mode 6	5.77	0.82	2.67	9.03	8.14	0.40	6.88	10.02
Aβ16	10.64	1.57	4.45	15.46	8.23	0.77	6.80	13.24

Rg values are also shown in Figure 3 and Table 5, and broadly mirror the trends seen in RMSD where the free peptide has the highest sd and maximum values (sd 0.77 and Max 13.24 Å), which reflects the flexibility of the metal-free peptide. However, binding modes 5 and 6, in which Zn coordinates to middle residues of the peptide (Glu11, His6,13, and14) and leaving the N-termini residues unbinding, show the highest mean values that approach or exceed that seen for the metal-free peptide, albeit with smaller maxima and standard deviations. Mean Rg for binding modes 1 to 4 are smaller than the free peptide, with binding modes 1 and 3 particularly compact. The mean value for 1-3 binding modes of Zn(II)-Aβ in which one of the coordinates is served by Asp1 or Glu3 and addition to binding mode 4 where the Zn bound to Nδ of His rings agree well with the experimental value of 7.4±0.2 Å.[15] For the free peptide, a theoretical approach for the calculation of Rg[86,87] from molecular weight $M_r = 1995$ yields $R_g = 9.35$ Å, in reasonable agreement with the simulated value of 8.23 ± 0.8 Å. Another experimental study of Aβ aggregation using hydrodynamic radii (R_h) reported by size exclusion chromatography and NMR found Zn complexes to be more compact and structured than metal-free peptide, in which R_h value of Aβ upon Zn(II) binding is 11.4 Å,[88] which fits well with our values.

Comparison of aMD data for binding mode 6 with that for conventional MD indicates that the former explores more conformational space than the latter, with larger sd and maximum value leading to a slightly larger mean value of Rg. However, accelerated MD cannot access smaller conformations, with both simulations having almost identical minimum Rg values. This lends

confidence that the aMD protocol and boost potential used result in realistic conformations and enhanced sampling of other binding modes.

Calculated RMSF of free Aβ-16 and metal bound complexes (Figure 4) follow a similar pattern to RMSD and Rg, with the lowest values for Zn(II) and the largest values for free peptide. However, binding mode 5 has the highest Lys16 and amidated cap mobility, which may explain the high Rg value of this mode. Metal-binding residues (Asp1, His6/14/13, Glu3, and Glu11) present minimal RMSF values, indicating how metal coordination limits their freedom of movement. In general, for all binding modes and free beta, C-terminal (Gln15, Lys16, and amidated cap), as well as Asp7 and Tyr10 residues, exhibit the greatest flexibility; N-terminus of free Aβ-16 has high RMSF value, but when bound to metal; Zn(II) this shows less positional mobility. Metals themselves (residue 18) have low RMSF, with binding modes 1 and 3 exhibiting particularly low mobility. Those two modes also showed lower RMSD mean vales.
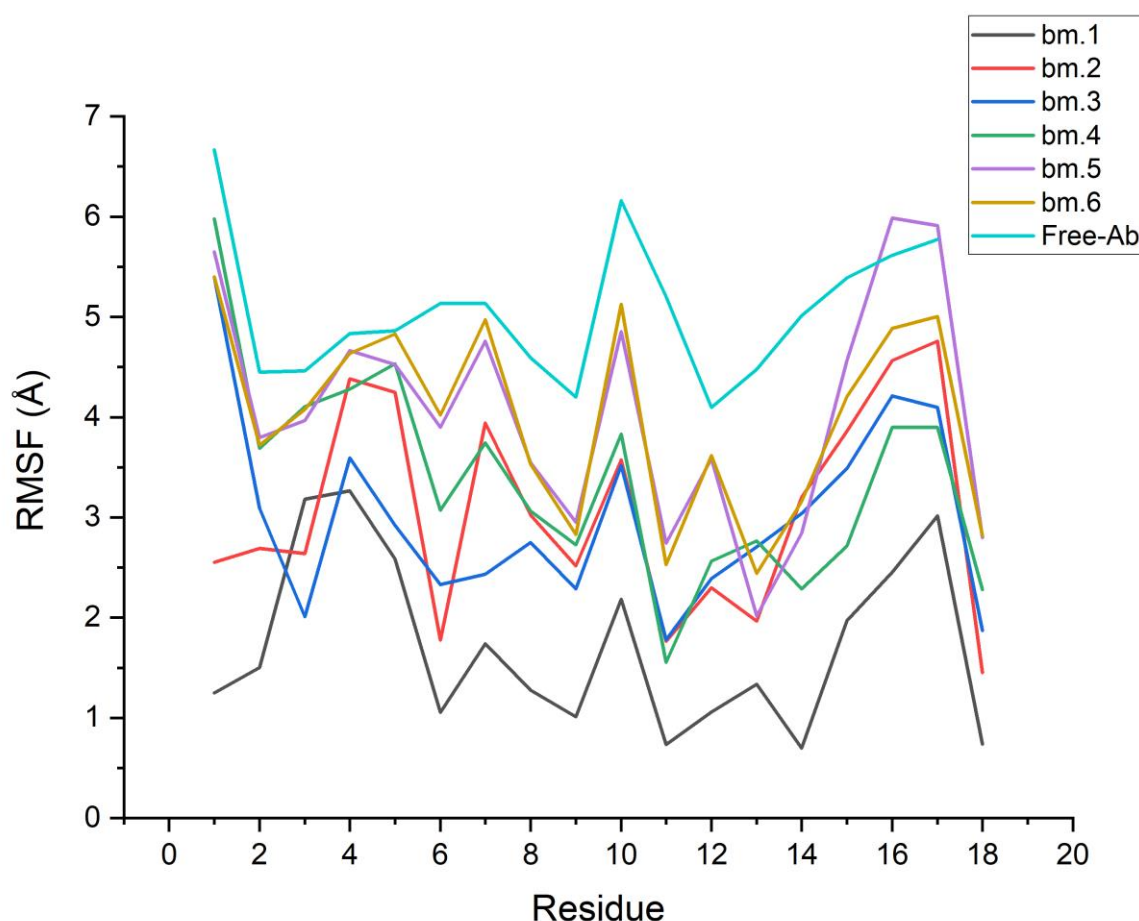

Figure 4 RMSF of each residue of free and Zn-bound Aβ-16. The metal ion itself is denoted residue 18, and the C-terminal amidated cap residue 17.

Clustering analysis of equilibrated trajectories on the basis of backbone dihedrals was used to extract key structural motifs: ribbon diagrams of the most representative clusters are shown in Figure 5 and Table 6. Binding mode 1 of Zn-(II)Aβ, which show the lowest Rg values, forms the lowest number of clusters with 3, of which one accounts for over 90% of frames, with the remaining clusters taking no more than 2%. Binding modes 2, 3, 4, and 6 form more clusters (16, 11, 20, and 15, respectively) with the most populated 14, 9, 16, and 29%, respectively. The most flexible, mode 5, forms 9 clusters with 60% of frames in the most populated one. Free Aβ-16 forms no clusters for which occupancy is more than 1% of total frames, providing further evidence for the flexibility of this peptide under these simulation conditions. Overall, the geometries of most populated clusters present tetrahedral shape around Zn.

Table 6 Cluster analysis data for equilibrated trajectories.

Clusters	# clusters	Most populated	2nd populated
Mode 1	3	93%	2%
Mode 2	16	14%	12%
Mode 3	11	9%	7%
Mode 4	20	16%	8%
Mode 5	9	60%	18%
Mode 6	15	29%	17%

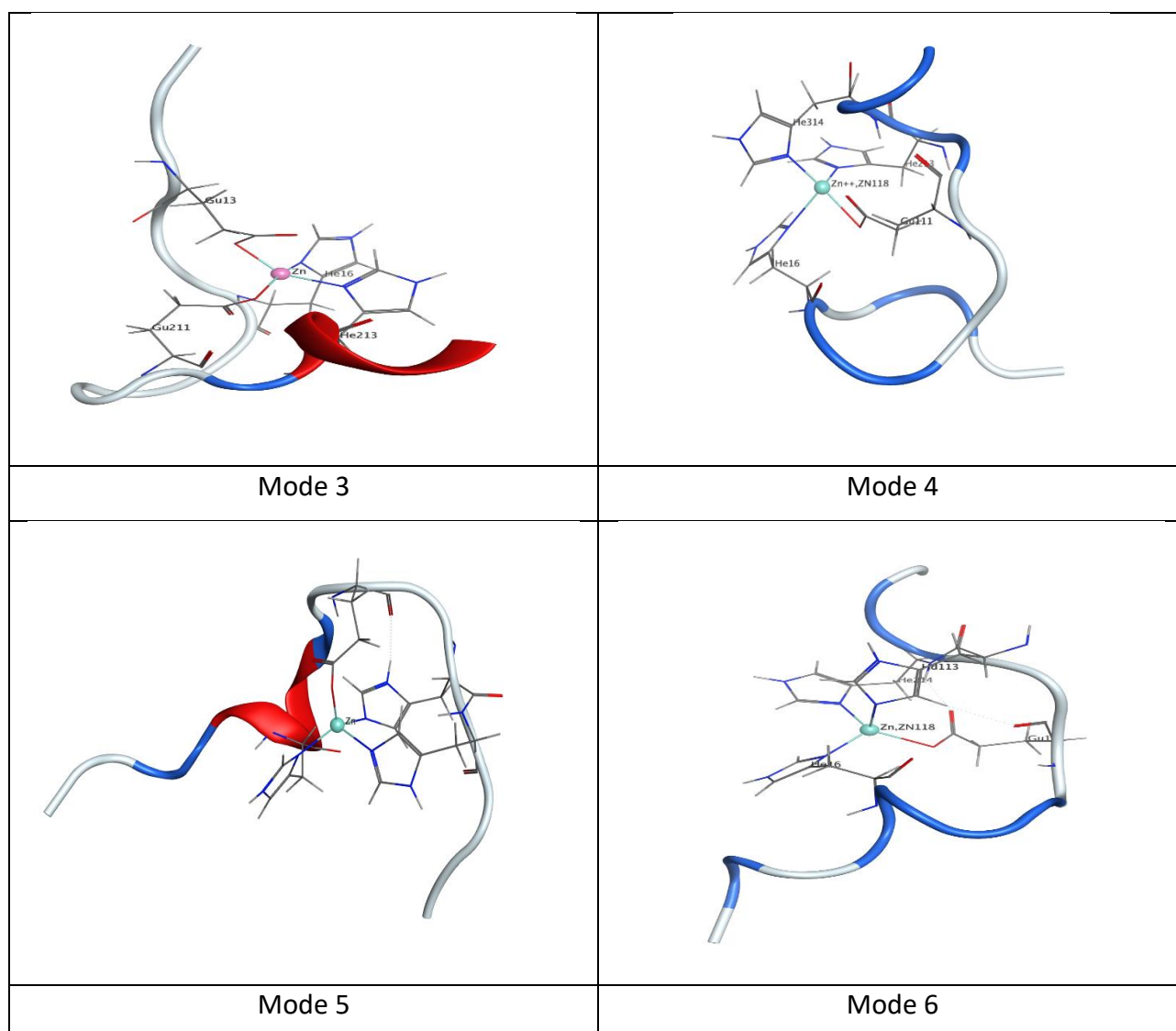| Mode 1 | Mode 2 |

| Mode 3 | Mode 4 |
| Mode 5 | Mode 6 |
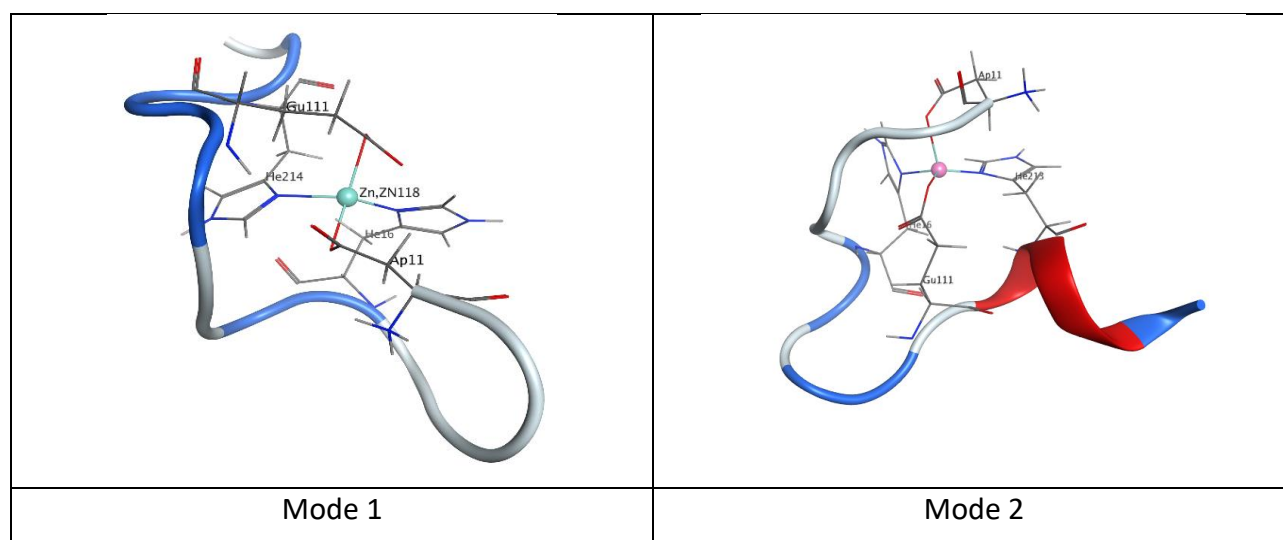
Figure 5 Ribbon diagram of the most populated clusters for Zn(II) and free AB.

To monitor the impact of metals binding on the secondary structure of Aβ peptides, we have performed secondary structure analysis of Aβ for all aMD trajectories (Figure 6 and Table 7). This shows that Aβ-16 adopts helical (both α- and 3_{10}-) conformations in 27% of frames, whereas Zn(II)-Aβ adopts more bend and turn structures, with a smaller abundance of helical structure in most binding modes and very small amounts of β-sheet. Monitoring of secondary structure over combined 600 ns trajectories shows that binding mode 1 of Zn(II)-Aβ maintains its structure without significant changes from the initial structure to the end of the simulation. Binding mode 2 shows more variation in structure and the only mode that shows 5 % of β-sheet folding and higher helical structure 12% comparing to other modes. Mode 2,3, and 6 show the highest percentage of helical structure among other modes. In contrast, free Aβ-16 is more varied suggesting a decreased abundance of defined secondary structuring in Aβ results from Zn binding.
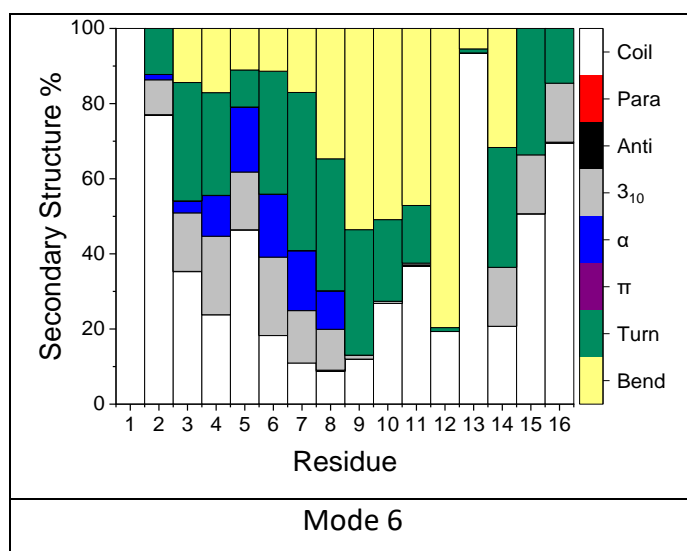
15

Aβ-16

Mode 1

Mode 2
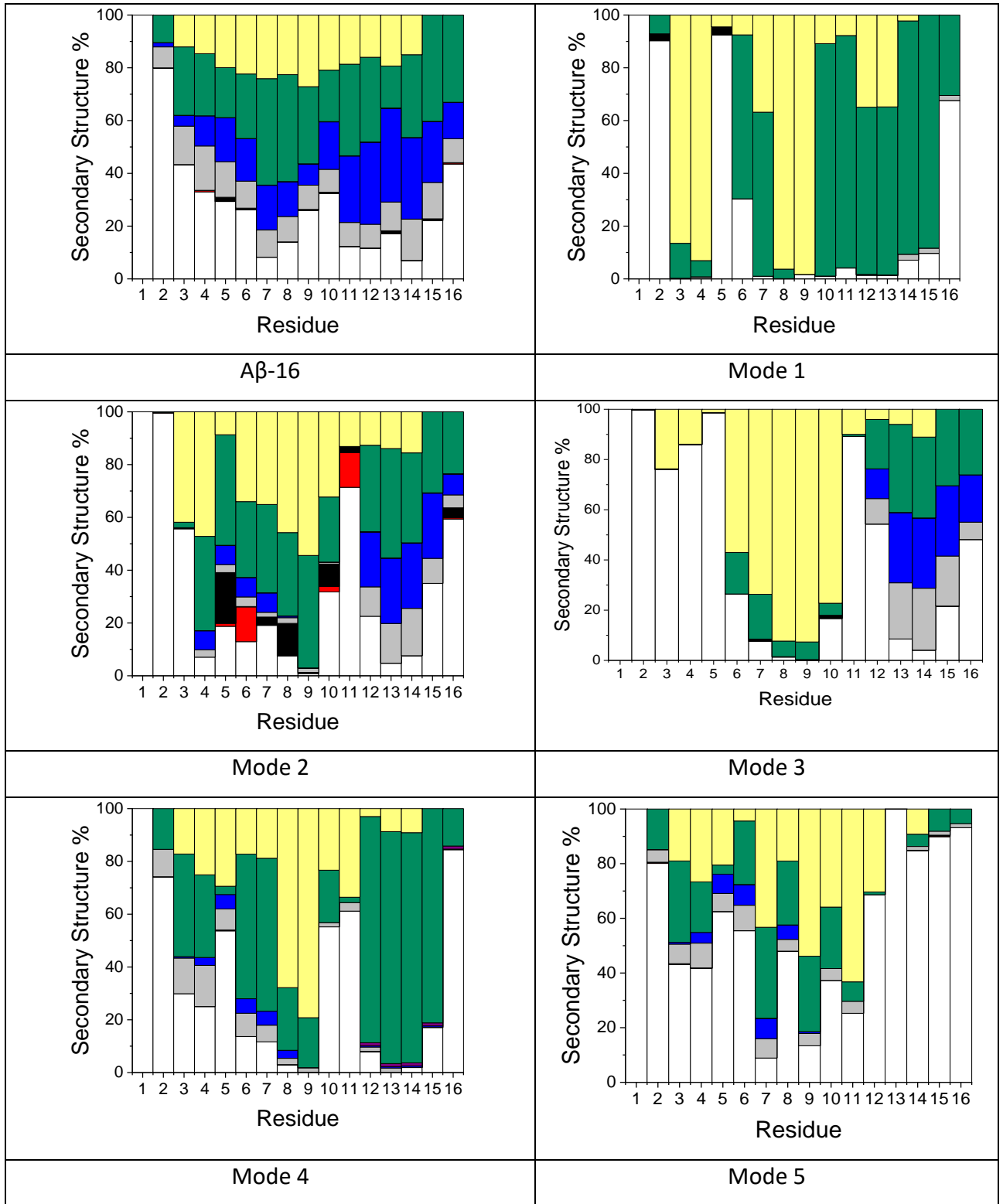
Mode 3

Mode 4

Mode 5

Figure 6 Secondary structure for Zn(II)-Aβ and free Aβ-16.

Table 7 Total secondary structure percentages for each system (%).

	Helix	Sheet	Other
experiment	**33.0**	**0.0**	**66.7**
Mode 1	0.5	0.3	99.2
Mode 2	13.0	5.0	82.0
Mode 3	12.5	0.2	87.4
Mode 4	6.6	0.1	93.3
Mode 5	6.2	0.1	93.7
Mode 6	14.5	0.1	85.4
Aβ-16	27.2	0.4	72.4

Ramachandran maps were used to explore the backbone structure Figure 7. All simulations give rise to the majority of frames in the broad general region of a right-handed helix. Free Aβ-16 has most residues in the region characteristic of a right handed helix, whereas Zn(II)-Aβ has a greater population of antiparallel β-sheet form and the greatest found in Mode 5, and also left-handed helical structures are shown in binding mode number 1. Closer inspection shows that two aMD simulations out of three for Zn(II)-Aβ lead to a population of this region.
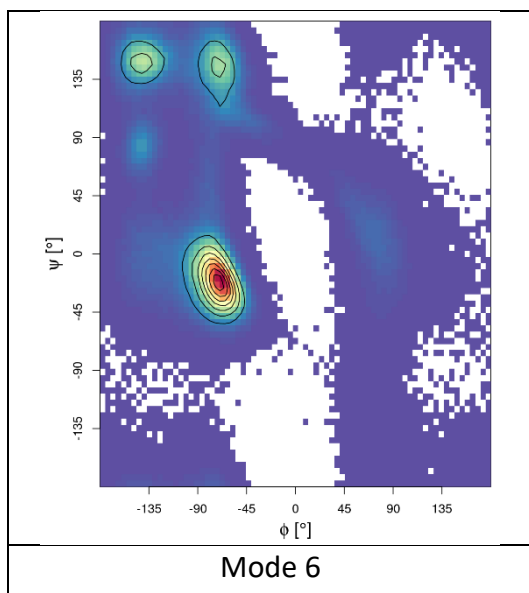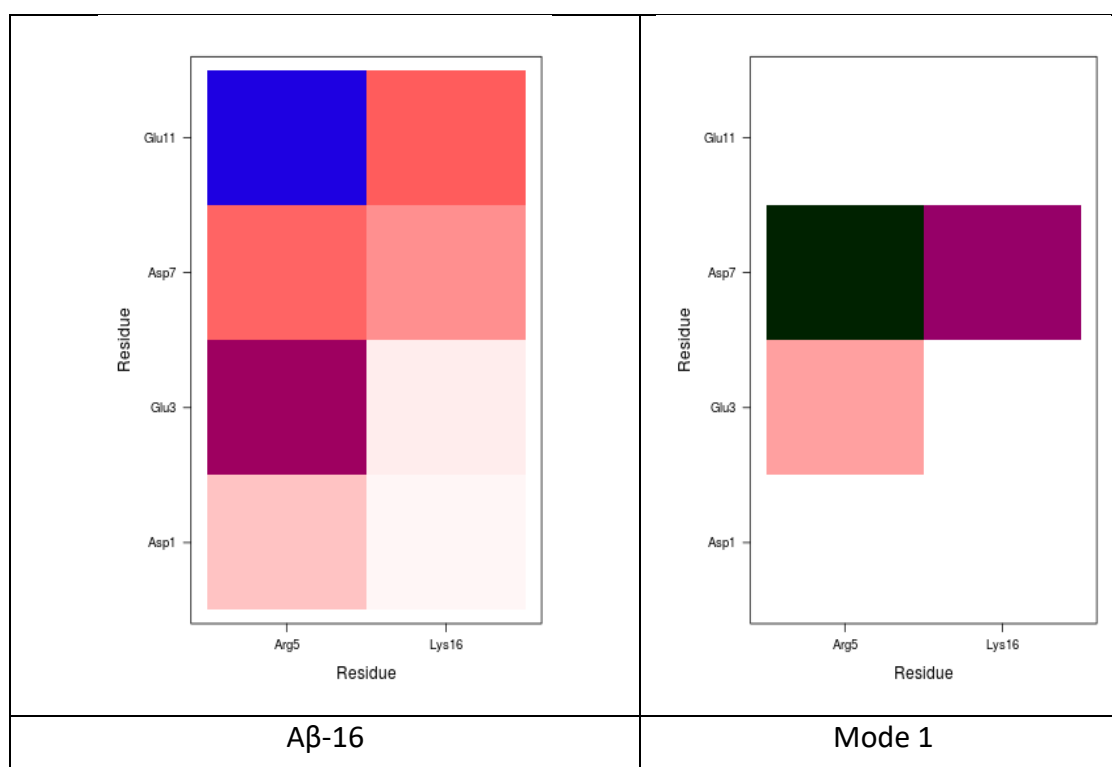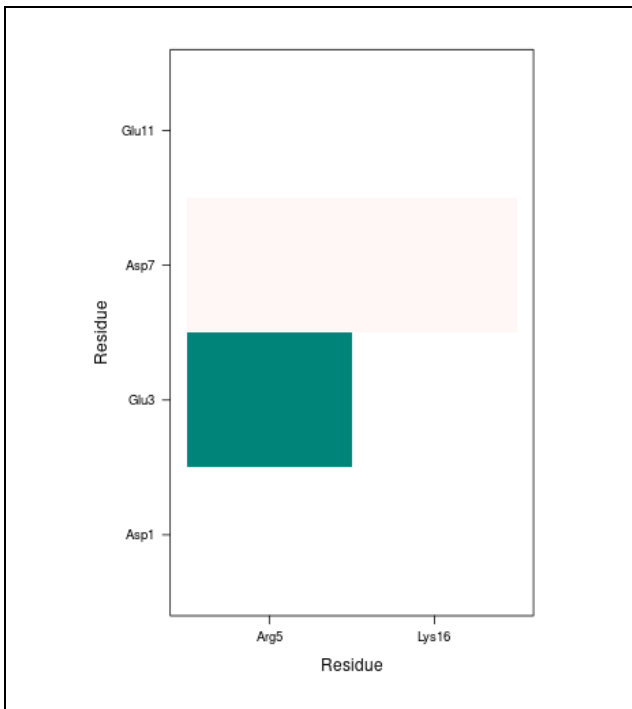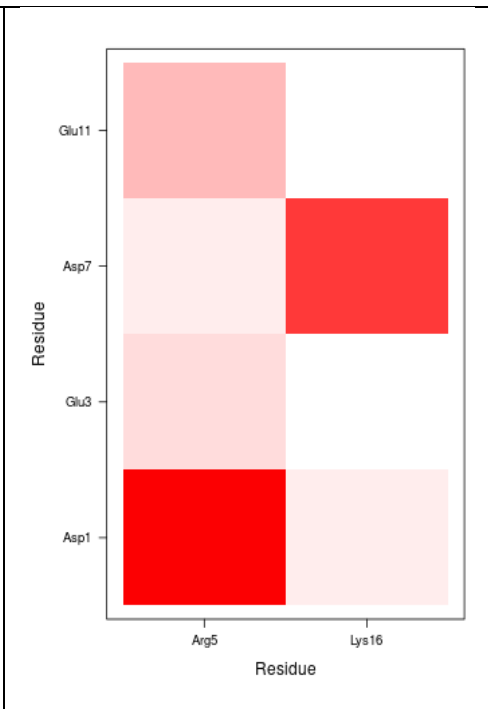
Aβ-16

Mode 1

Mode 2

Mode 3

Mode 4

Mode 5

Mode 6
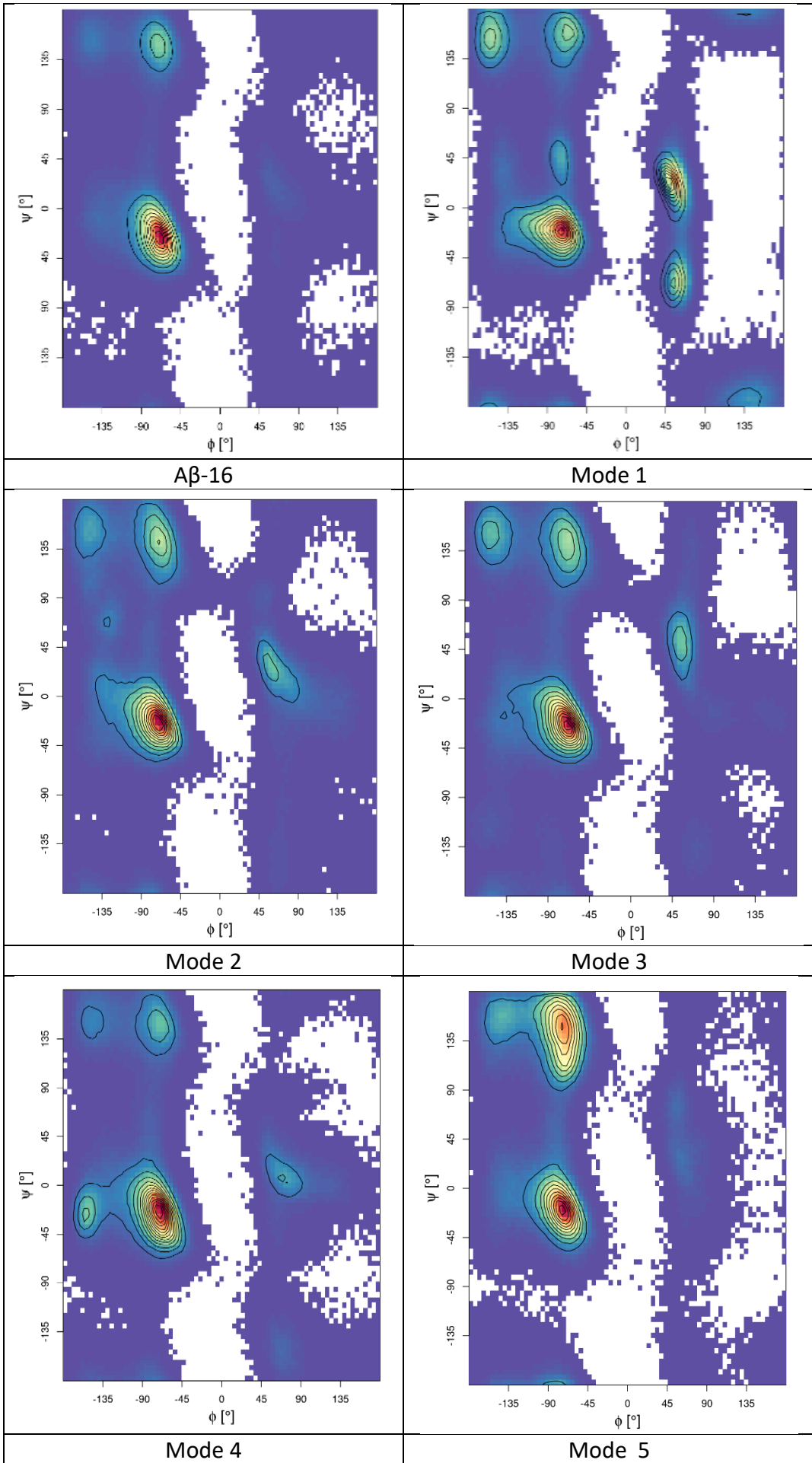
Figure 7 Ramachandran maps for Zn(II)-Aβ and free Aβ-16.

The prevalence of salt-bridge contacts is shown in Figure 8 (numerical data can be found in Supporting Information). Most of the binding modes, except mode 2, of Zn(II)-Aβ show strong contact between Asp7 and Arg5, especially mode 1 in almost 100% of frames, and also 40% between Asp7 and Lys16 in modes 1 (which show low RMSD and Rg), but no contact at all between Arg5 and Glu 11 in most of binding modes but weak interaction that seen in Mode 3 less than 5%. For mode 2, there are few contacts except strong interaction between Glu3 and Arg5. Free Aβ-16 shows many more salt-bridges but with lower occupancy, with only Arg5-Glu11 being present for over 50% of frames.
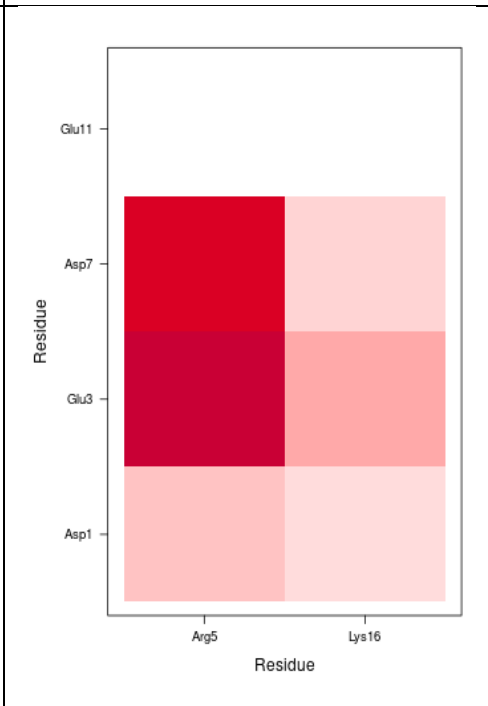

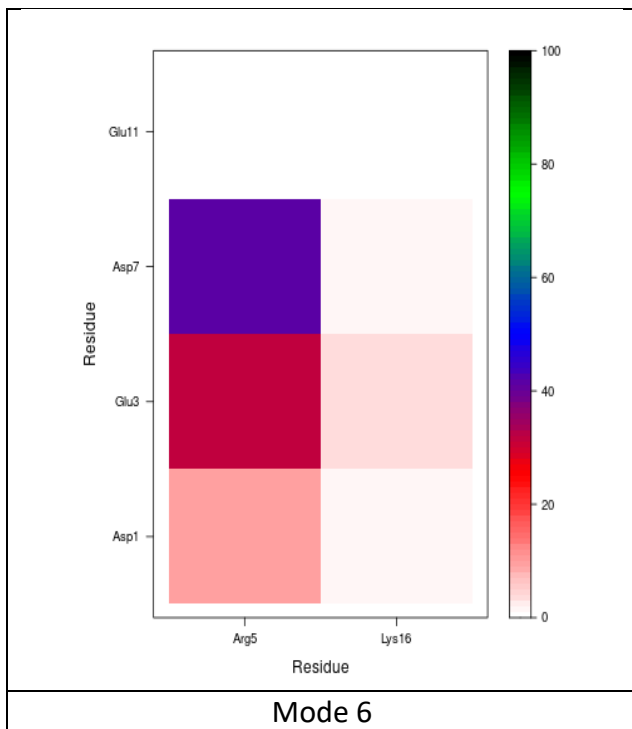| Aβ-16 | Mode 1 |

|	
Mode 2	Mode 3
Mode 4	Mode 5

Mode 6
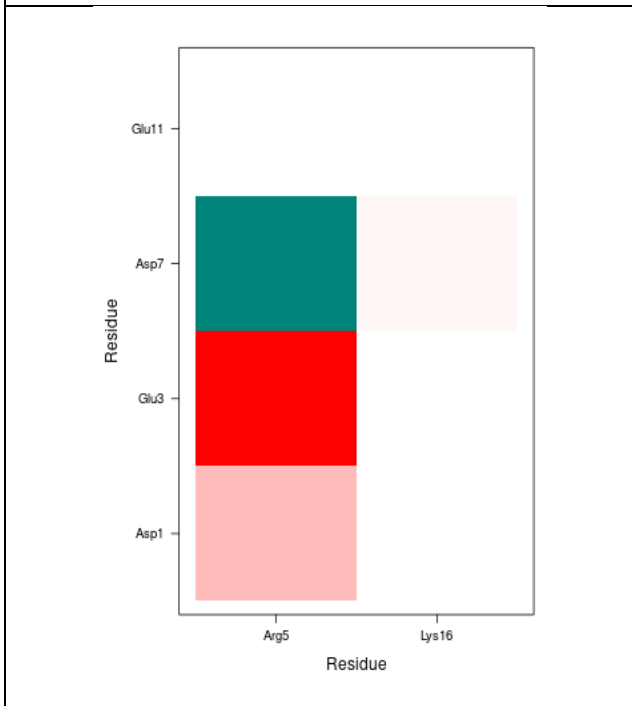
Figure 8 Salt bridge maps of Zn(II)-Aβ and free Aβ-16.

Contact maps showing the average distance between residue pairs are shown in Figure 9 for binding mode 1 and free peptide (maps for all other binding modes can be found in SI). This makes it clear that free Aβ-16 shows less interaction between distant residues than the Zn complex, with long distances between N and C-termini reflecting the flexibility of the peptide in absence of metal effects. Zn(II)-Aβ shows shorter distances between N- and C-termini, and also short contacts between specific residues. These are primarily involved in metal binding (His6-His14, His6-Glu11) but other close contacts are also evident (Asp1-Gly9, Glu11-Gln15), reflecting the profound effect of Zn binding on the structural flexibility compared to the free peptide.
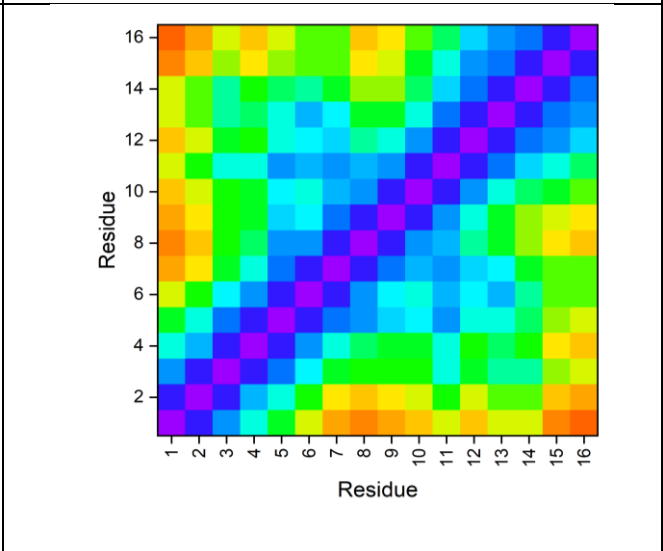
Aβ-16

Mode 1

Mode 2

Mode 3

Mode 4

Mode 5

| | Mode 6 |
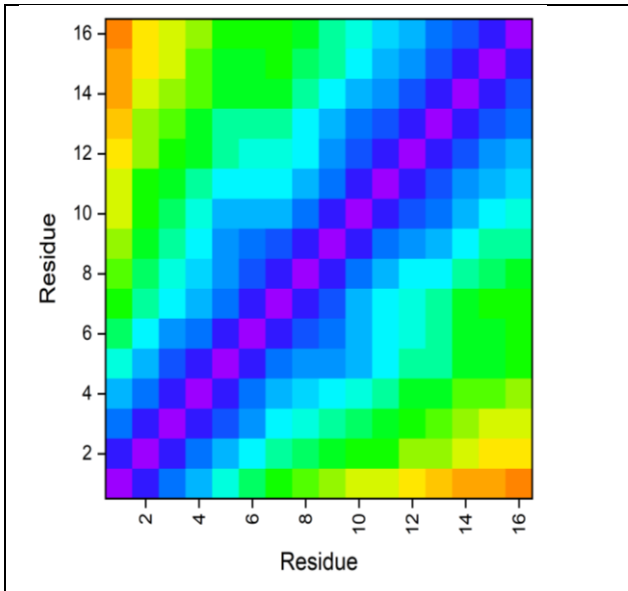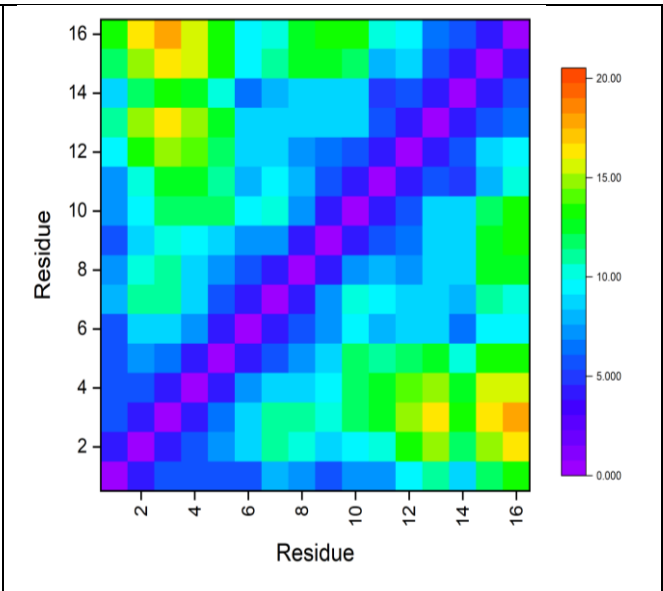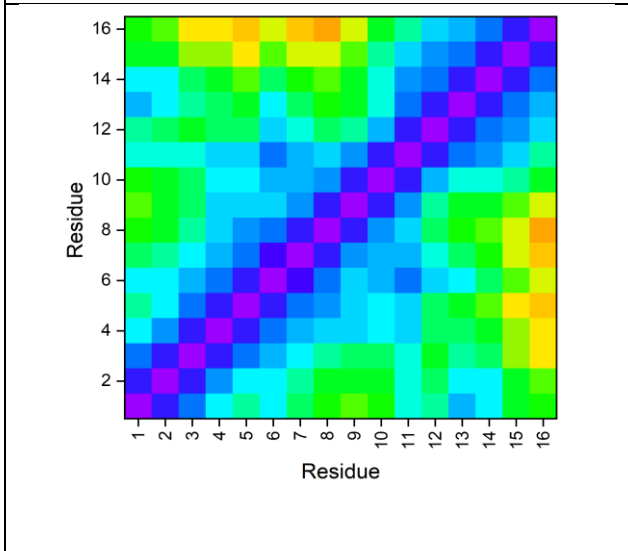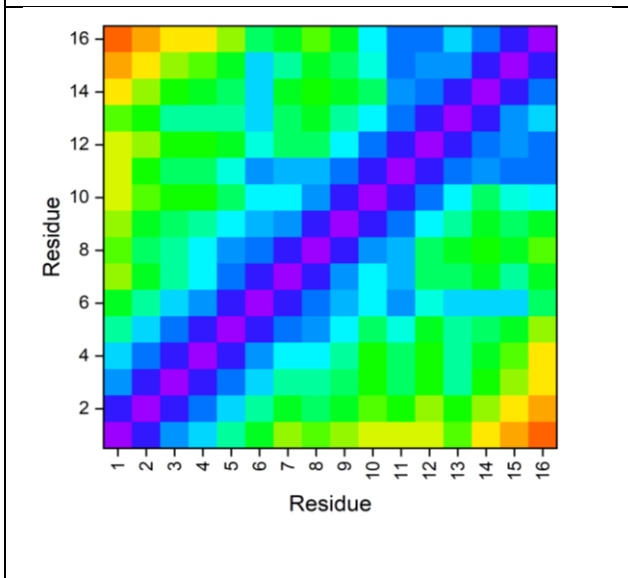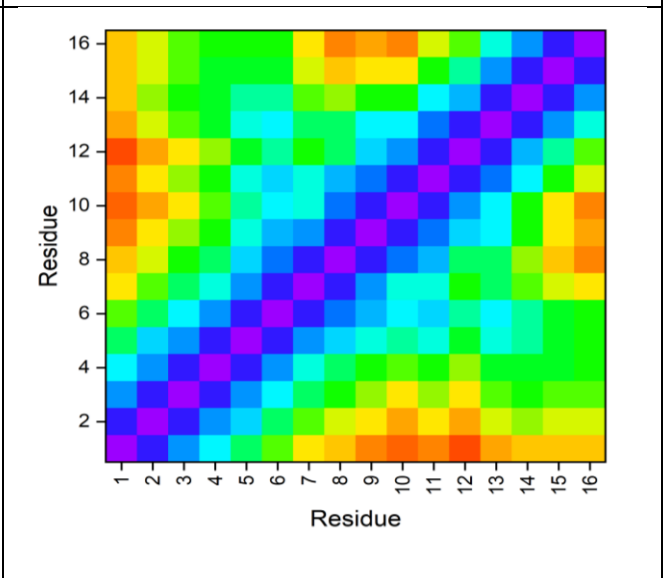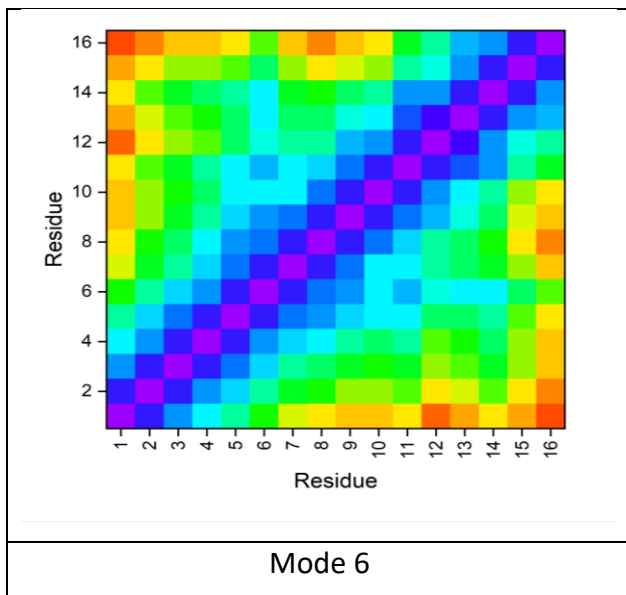
Figure 9 Contact map of binding modes of Zn(II)-Aβ and free Aβ-16.

Hydrogen bond formation is an important factor for the dynamics and stabilization of proteins. The number of H-bonds formed between residues is shown in Table 8. This shows that Zn(II)-Aβ of all modes and free Aβ-16 exhibit very similar patterns of hydrogen bonding, each with a mean of *ca.*5 and a maximum of 15 in some frames. The most persistent H-bonds are 45 and 49 % for binding mode 1 and 6 form between His14 (donor) and Glu11 (acceptor) with a percentage of 45 and 49%, respectively, but just 16% for Aβ-16 intra-residue H-bond within Glu3. Mode 3 and 5 show the maximum number of hydrogen bonds with 11 only which is less than other modes. This data also shows that every aMD simulation visits at least some frames in which no hydrogen bonds are present.

Table 8 HB count for Zn(II)-Aβ and free Aβ-16.

Number of HB	Mean	sd	Max	Min
Mode 1	5.08	1.94	14	0
Mode 2	3.71	1.70	13	0
Mode 3	3.65	1.67	11	0
Mode 4	4.74	1.85	14	0
Mode 5	3.77	1.68	11	0
Mode 6	4.50	1.77	14	0
Aβ-16	5.14	1.98	15	0

The tables below include a summary of the conventional and accelerated MD results, for the systems using ff14SB, for binding mode 6. Rg data shows that aMD samples a greater range of molecular size, with a maximum Rg of more than 1 Å greater than conventional MD, with notably larger mean and sd values. The secondary structure of the peptide remains rather similar between cMD and aMD, especially when looking at the β-sheet character which is low in both cases, whereas helical content is higher in conventional MD. Both methods sample conformations with no helix or sheet (100% other), with aMD spending more time in such conformations. Hydrogen bond counts are also similar between sampling methods: both methods sample conformations with no H-bonds and others with 14, although the mean value from aMD is slightly smaller. Taken together, this gives a picture of aMD leaving potential energy wells more quickly than conventional MD, visiting more extended conformations with less defined secondary structure more often before collapsing again to more compact conformations, as required for proper sampling of a flexible peptide such as Aβ.

Table 9 Comparison of conventional and accelerated MD for binding mode 6

	Mean	Sd	Max	Min
Rg cMD	7.58	0.24	9.05	6.78
aMD	8.14	0.40	10.02	6.88
Helix % cMD	27.4	29.3	90.6	0.0
aMD	14.5	13.0	37.7	0.0
Sheet % cMD	0.5	1.2	3.5	0.0

aMD	0.1	0.1	0.3	0.0
Other % cMD	72.1	28.8	100.0	9.4
aMD	85.4	12.9	100.0	62.4
H-bond cMD	6.17	1.89	14	0
aMD	4.50	1.77	14	0

Reweighting of the accelerated MD boost potential allows reconstruction of the free energy surface. Figure 10 shows 1D free energy as a function of hydrogen bond count and end-to-end distance (R_{E-E}), defined as the distance between the N-terminal and C-terminal $C\alpha$ atoms, for binding mode 1 and free peptide (all binding modes can be found in SI). This shows broad minima centred on 4 or 5 H-bonds for both the Zn complexes and the free peptide. A second low free energy state is found about 2 kcal mol^{-1} at 13 H-bonds for free Aβ-16 peptide, reflecting the greater number of these interactions in this more flexible system. A large range of R_{E-E} is accessible at low energy: for Zn, the lowest energy lies at around 13 Å, but values of between 6 and 16 Å are within 5 kcal mol^{-1} of this minimum. In comparison, the metal-free peptide shows the minimum ranged within a wider distance from 5 to around 40 Å and the lowest located at ca.14 Å in which lies at a similar place as the minima of Zn.
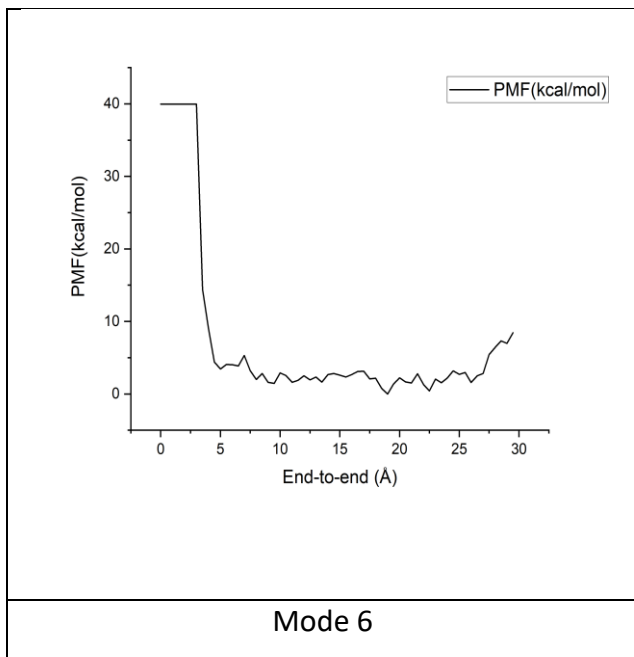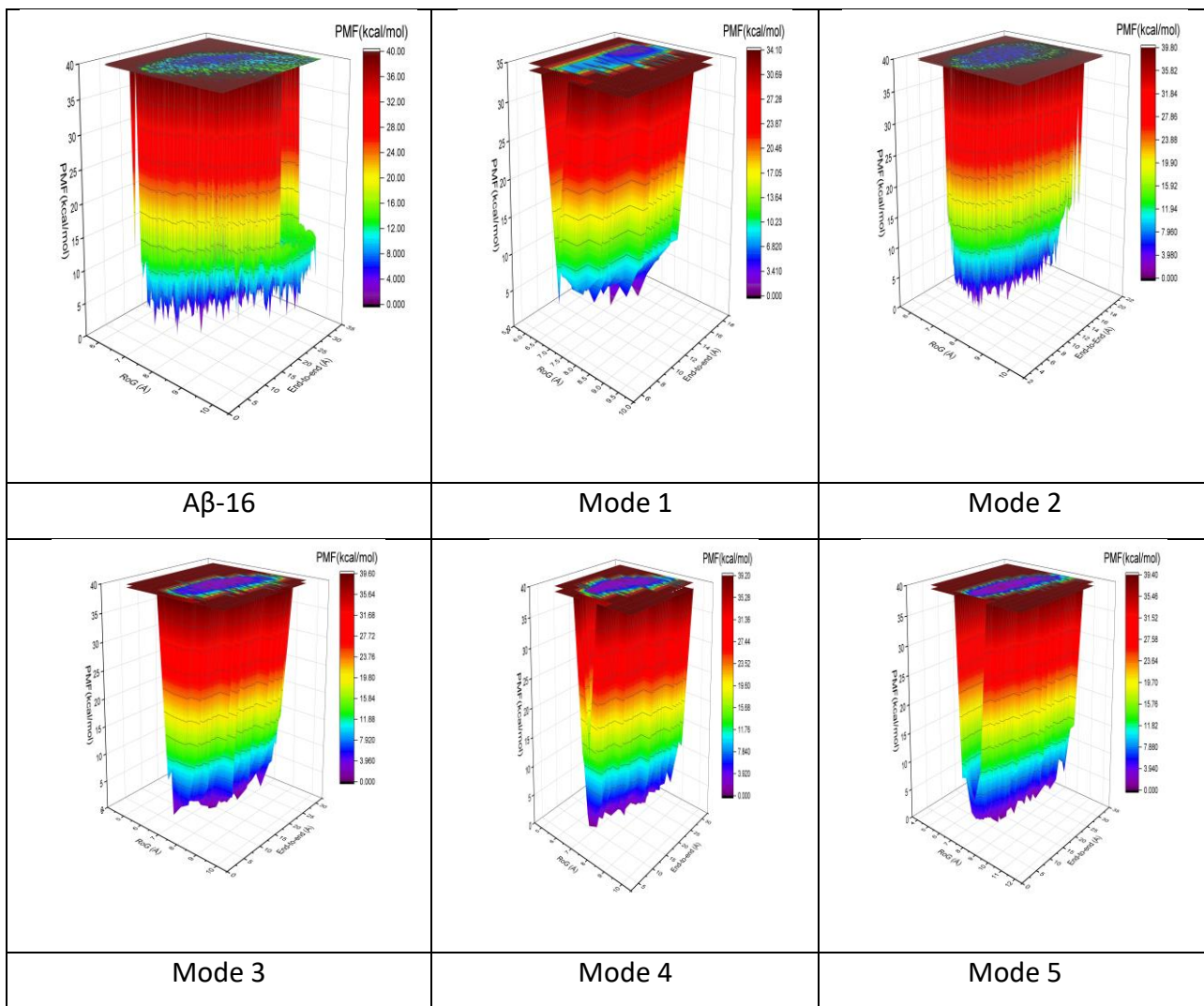
Aβ-16

Mode 1

Mode 2

Mode 3

Mode 4

Mode 5

Mode 6
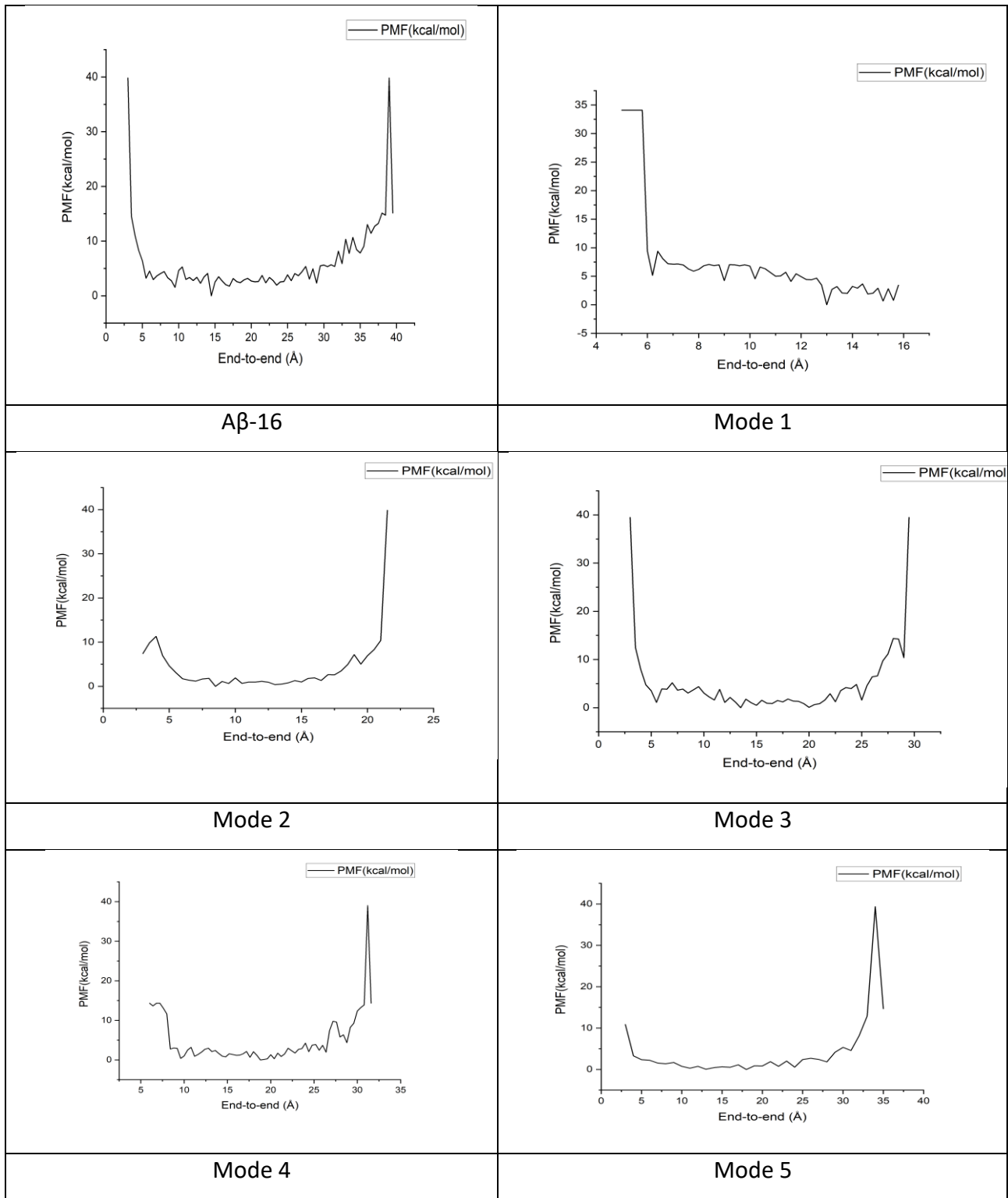
Figure 10 1D-Free energy surface of binding modes of Zn(II)-Aβ and free Aβ-16 as a function of end-to-end distance (Å)

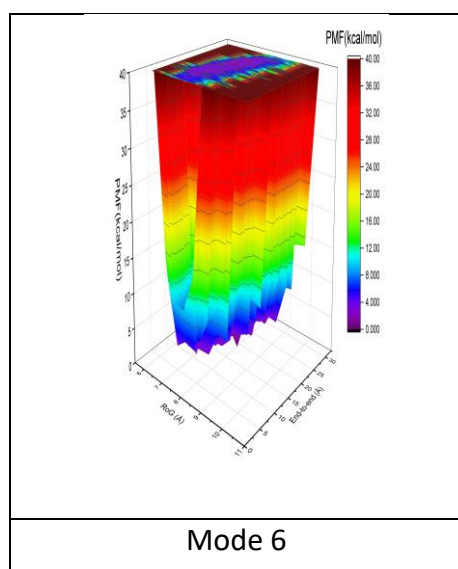| Aβ-16 | Mode 1 | Mode 2 |
| Mode 3 | Mode 4 | Mode 5 |

Mode 6

Figure 11 2D free energy landscapes as a function of end-to-end distance and Rg (Å) Zn(II)-Aβ and free Aβ-16 (kcal/mol).

2D free energy surfaces were calculated using the radius of gyration and end-to-end distance (Figure 11). This shows that the favourable structures of free Aβ16 have many different R_{E-E} but a much narrower range of Rg. Without metal, R_{E-E} varies from 6 to 30 Å, with the most stable of these found around 15-25 Å. Binding modes 1, 2, and 3 of Zn(II) bound to the beginning of Aβ-16 residues (Asp1, or Glu3) reduces the R_{E-E} range dramatically due to the constrained of N-terminus, an aspect also evident in RMSF data, whereas binding modes 4, 5, and 6 in which Zinc bound to His 6, 13 and 14 in the centre of the peptide can access a much wider range of R_{E-E}, nearer to free peptide values. These results demonstrate that transitions between the structures located in the most stable basins require the overriding of large energy barriers more than 2 kcal mol^{-1} for metal binding and more than 6 kcal mol^{-1} for free Aβ.

Conclusions

We have explored the performance of different forcefields and solvent models for the description of Zn(II) bound to Aβ1-16 by comparing the results of 100 ns conventional MD with the ensemble of 20 NMR structures reported as PDB entry 1ZE9. We find that implicit solvent models give better reproduction of overall size and shape, measured by radius of gyration and globularity, compared to explicit solvent. Secondary structure is also well reproduced by some forcefields with implicit solvent, with ff14SB performing particularly well. In contrast, no combination of forcefield and solvent model is found to satisfactorily reproduce all aspects of salt bridges, although some do well for some of the more common interactions found in the experiment. Taken together, we conclude

that ff14SB with the default GBSA model is at least as good a choice as any other since our chief interest is in the size and secondary structure of metal complexes of Aβ.

Accelerated MD enhances sampling by flattening the hills and ridges on energy surfaces which can prevent conventional MD from accessing certain states. We performed aMD to explore the structures of Aβ1-16 and its complex with Zn(II). Our data show that the metal ion reduces the flexibility of the peptide, and significantly alters the pattern of salt bridges, but affects hydrogen bond interactions rather less. Our simulation of different binding modes of Aβ-16 bound to Zn(II) shows that variation in specific atoms/residues involved in binding affects results in respect of secondary structure, clusters, salt bridge, RMSF and compactness. Here, the modes where the first residues of N- terminal side coordinated to Zn(II) are more compact and restricted peptides. However, in the cases where the Zn(II) coordinated to two His rings and two carboxylate groups those located on the middle of Aβ-16 chain are less constrained and more flexible ensembles.

Acknowledgments

References

1   J. F. Dartigues, Alzheimer's disease: a global challenge for the 21st century, *Lancet Neurol.*, 2009, **8**, 1082–1083.

2   W. P. Esler, E. R. Stimson, J. M. Jennings, J. R. Ghilardi, P. W. Mantyh and J. E. Maggio, Zinc-Induced Aggregation of Human and Rat β-Amyloid Peptides In Vitro, *J. Neurochem.*, 2002, **66**, 723–732.

3   A. I. Bush, W. H. Pettingell, G. Multhaup, M. D. Paradis, J. P. Vonsattel, J. F. Gusella, K. Beyreuther, C. L. Masters and R. E. Tanzi, Rapid induction of Alzheimer Aβ amyloid formation by zinc, *Science (80-.).*, 1994, **265**, 1464–1467.

4   X. Huang, C. S. Atwood, R. D. Moir, M. A. Hartshorn, R. E. Tanzi and A. I. Bush, Trace metal contamination initiates the apparent auto-aggregation, amyloidosis, and oligomerization of Alzheimer's Aβ peptides, *J. Biol. Inorg. Chem.*, 2004, **9**, 954–960.

5   K. P. Kepp, Bioinorganic chemistry of Alzheimer's disease, *Chem. Rev.*, 2012, **112**, 5193–5239.

6   K. I. Silva, B. C. Michael, S. J. Geib and S. Saxena, ESEEM Analysis of Multi-Histidine Cu(II)-

Coordination in Model Complexes, Peptides, and Amyloid-β, *J. Phys. Chem. B*, 2014, **118**, 8935–8944.

7   A. I. Bush, The metallobiology of Alzheimer's disease, *Trends Neurosci.*, 2003, **26**, 207–214.

8   M. . Lovell, J. . Robertson, W. . Teesdale, J. . Campbell and W. . Markesbery, Copper, iron and zinc in Alzheimer's disease senile plaques, *J. Neurol. Sci.*, 1998, **158**, 47–52.

9   C. C. Curtain, F. E. Ali, D. G. Smith, A. I. Bush, C. L. Masters and K. J. Barnham, Metal ions, pH, and cholesterol regulate the interactions of Alzheimer's disease amyloid-β peptide with membrane lipid, *J. Biol. Chem.*, 2003, **278**, 2977–2982.

10   L. Guilloreau, L. Damian, Y. Coppel, H. Mazarguil, M. Winterhalter and P. Faller, Structural and thermodynamical properties of CuII amyloid-β16/28 complexes associated with Alzheimer's disease, *J. Biol. Inorg. Chem.*, 2006, **11**, 1024–1038.

11   J. W. Karr, H. Akintoye, L. J. Kaupp and V. A. Szalai, N-terminal deletions modify the Cu2+ binding site in amyloid-β, *Biochemistry*, 2005, **44**, 5478–5487.

12   T. Kowalik-Jankowska, M. Ruta, K. Wiśniewska and L. Łankiewicz, Coordination abilities of the 1-16 and 1-28 fragments of β-amyloid peptide towards copper(II) ions: A combined potentiometric and spectroscopic study, *J. Inorg. Biochem.*, 2003, **95**, 270–282.

13   S. Bolognin, L. Messori, D. Drago, C. Gabbiani, L. Cendron and P. Zatta, Aluminum, copper, iron and zinc differentially alter amyloid-Aβ 1-42 aggregation and toxicity, *Int. J. Biochem. Cell Biol.*, 2011, **43**, 877–885.

14   T. Kowalik-Jankowska, M. Ruta-Dolejsz, K. Wiśniewska and L. Lankiewicz, Cu(II) interaction with N-terminal fragments of human and mouse β-amyloid peptide, *J. Inorg. Biochem.*, 2001, **86**, 535–545.

15   S. Zirah, S. A. Kozin, A. K. Mazur, A. Blond, M. Cheminant, I. Ségalas-Milazzo, P. Debey and S. Rebuffat, Structural Changes of Region 1-16 of the Alzheimer Disease Amyloid β-Peptide upon Zinc Binding and *in Vitro* Aging, *J. Biol. Chem.*, 2006, **281**, 2151–2161.

16   A. I. Bush and R. E. Tanzi, Therapeutics for Alzheimer's disease based on the metal hypothesis, *Neurotherapeutics*, 2008, **5**, 421–432.

17   Y. H. Hung, A. I. Bush and R. A. Cherny, Copper in the brain and Alzheimer's disease, *J. Biol. Inorg. Chem.*, 2010, **15**, 61–76.

18   K. J. Barnham and A. I. Bush, Metals in Alzheimer's and Parkinson's Diseases, *Curr. Opin. Chem. Biol.*, 2008, **12**, 222–228.

19   T. Lynch, R. A. Cherny and A. I. Bush, Oxidative processes in Alzheimer's disease: The role of Aβ-metal interactions, *Exp. Gerontol.*, 2000, **35**, 445–451.

20   K. J. Barnham, C. L. Masters and A. I. Bush, Neurodegenerative diseases and oxidatives stress, *Nat. Rev. Drug Discov.*, 2004, **3**, 205–214.

21   X. Zhu, B. Su, X. Wang, M. A. Smith and G. Perry, Causes of oxidative stress in Alzheimer disease, *Cell. Mol. Life Sci.*, 2007, **64**, 2202–2210.

22   V. Desai and S. G. Kaler, Role of copper in human neurological disorders, *Am. J. Clin. Nutr.*, 2008, **88**, 855–858.

23   C. Cheignon, M. Tomas, D. Bonnefont-Rousselot, P. Faller, C. Hureau and F. Collin, Oxidative stress and the amyloid beta peptide in Alzheimer's disease, *Redox Biol.*, 2018, **14**, 450–464.

24   E. Atrián-Blasco, A. Conte-Daban and C. Hureau, Mutual interference of Cu and Zn ions in Alzheimer's disease: Perspectives at the molecular level, *Dalt. Trans.*, 2017, **46**, 12750–12759.

25   M. A. Greenough, J. Camakaris and A. I. Bush, Metal dyshomeostasis and oxidative stress in Alzheimer's disease, *Neurochem. Int.*, 2013, **62**, 540–555.

26   A. Georgi, M. Velasco Polo, K. Crincoli, K. Mackenzie and F. D. Kopinke, Accelerated Catalytic Fenton Reaction with Traces of Iron: An Fe-Pd-Multicatalysis Approach, *Environ. Sci. Technol.*, 2016, **50**, 5882–5891.

27   R. Rajendran, R. Minqin, M. D. Ynsa, G. Casadesus, M. A. Smith, G. Perry, B. Halliwell and F. Watt, A novel approach to the identification and quantitative elemental analysis of amyloid deposits-Insights into the pathology of Alzheimer's disease, *Biochem. Biophys. Res. Commun.*, 2009, **382**, 91–95.

28   K. Pauwels, T. L. Williams, K. L. Morris, W. Jonckheere, A. Vandersteen, G. Kelly, J. Schymkowitz, F. Rousseau, A. Pastore, L. C. Serpell and K. Broersen, Structural basis for increased toxicity of pathological Aβ42:Aβ40 ratios in alzheimer disease, *J. Biol. Chem.*, 2012, **287**, 5650–5660.

29   S. Zirah, S. Rebuffat, S. A. Kozin, P. Debey, F. Fournier, D. Lesage and J.-C. Tabet, Zinc binding properties of the amyloid fragment Aβ(1–16) studied by electrospray-ionization mass spectrometry, *Int. J. Mass Spectrom.*, 2003, **228**, 999–1016.

30   S. A. Kozin, S. Zirah, S. Rebuffat, G. Hui Bon Hoa and P. Debey, Zinc Binding to Alzheimer's Aβ(1–16) Peptide Results in Stable Soluble Complex, *Biochem. Biophys. Res. Commun.*, 2001, **285**, 959–964.

31   M. Rana and A. K. Sharma, Cu and Zn interactions with Aβ peptides: consequence of coordination on aggregation and formation of neurotoxic soluble Aβ oligomers, *Metallomics*, 2019, **11**, 64–84.

32   J. Nasica-Labouze, P. H. Nguyen, F. Sterpone, O. Berthoumieu, N.-V. Buchete, S. Coté, A. De

Simone, A. J. Doig, P. Faller, A. Garcia, A. Laio, M. S. Li, S. Melchionna, N. Mousseau, Y. Mu, A. Paravastu, S. Pasquali, D. J. Rosenman, B. Strodel, B. Tarus, J. H. Viles, T. Zhang, C. Wang and P. Derreumaux, Amyloid β Protein and Alzheimer's Disease: When Computer Simulations Complement Experimental Studies, *Chem. Rev.*, 2015, **115**, 3518–3563.

33   E. Gaggelli, A. Janicka-Klos, E. Jankowska, H. Kozlowski, C. Migliorini, E. Molteni, D. Valensin, G. Valensin and E. Wieczerzak, NMR Studies of the Zn2+ Interactions with Rat and Human β-Amyloid (1–28) Peptides in Water-Micelle Environment, *J. Phys. Chem. B*, 2008, **112**, 100–109.

34   G. Grasso and A. Danani, Molecular simulations of amyloid beta assemblies, *Adv. Phys. X*, 2020, **5**, 1770627.

35   B. Strodel and O. Coskuner-Weber, Transition Metal Ion Interactions with Disordered Amyloid-β Peptides in the Pathogenesis of Alzheimer's Disease: Insights from Computational Chemistry Studies, *J. Chem. Inf. Model.*, 2019, **59**, 1782–1805.

36   T. Marino, N. Russo, M. Toscano and M. Pavelka, On the metal ion (Zn2+, Cu2+) coordination with beta-amyloid peptide: DFT computational study, *Interdiscip. Sci. Comput. Life Sci.*, 2010, **2**, 57–69.

37   P. O. Tsvetkov, A. A. Kulikova, A. V. Golovin, Y. V. Tkachev, A. I. Archakov, S. A. Kozin and A. A. Makarov, Minimal Zn2+ Binding Site of Amyloid-β, *Biophys. J.*, 2010, **99**, L84–L86.

38   M. Turner, S. T. Mutter and J. A. Platts, Molecular dynamics simulation on the effect of transition metal binding to the N-terminal fragment of amyloid-β, *J. Biomol. Struct. Dyn.*, 2019, **37**, 4590–4600.

39   J. Alí-Torres, A. Mirats, J.-D. Maréchal, L. Rodríguez-Santiago and M. Sodupe, Modeling Cu2+-Aβ complexes from computational approaches, *AIP Adv.*, 2015, **5**, 92402.

40   L. Pan and J. C. Patterson, Molecular Dynamics Study of Zn(Aβ) and Zn(Aβ)2, *PLoS One*, 2013, **8**, 1–8.

41   P. D. Q. Huy, Q. Van Vuong, G. La Penna, P. Faller and M. S. Li, Impact of Cu(II) Binding on Structures and Dynamics of Aβ42 Monomer and Dimer: Molecular Dynamics Study, *ACS Chem. Neurosci.*, 2016, **7**, 1348–1363.

42   S. T. Mutter, R. J. Deeth, M. Turner and J. A. Platts, Benchmarking of copper(II) LFMM parameters for studying amyloid-β peptides, *J. Biomol. Struct. Dyn.*, 2018, **36**, 1145–1153.

43   M. Turner, J. A. Platts and R. J. Deeth, Modeling of Platinum-Aryl Interaction with Amyloid-β Peptide, *J. Chem. Theory Comput.*, 2016, **12**, 1385–1392.

44   A. K. Somavarapu and K. P. Kepp, The Dependence of Amyloid-β Dynamics on Protein Force

Fields and Water Models, *ChemPhysChem*, 2015, **16**, 3278–3289.

45   C. R. Watts, A. Gregory, C. Frisbie and S. Lovas, Effects of force fields on the conformational and dynamic properties of amyloid β(1-40) dimer explored by replica exchange molecular dynamics simulations, *Proteins Struct. Funct. Bioinforma.*, 2018, **86**, 279–300.

46   Z. Sun and X. Wang, Thermodynamics of Helix formation in small peptides of varying length in vacuo, implicit solvent and explicit solvent: Comparison between AMBER force fields, *J. Theor. Comput. Chem.*, 2019, **18**, 1–32.

47   R. Zhou, Free energy landscape of protein folding in water: Explicit vs. implicit solvent, *Proteins Struct. Funct. Genet.*, 2003, **53**, 148–161.

48   Q. Shao and W. Zhu, Assessing AMBER force fields for protein folding in an implicit solvent, *Phys. Chem. Chem. Phys.*, 2018, **20**, 7206–7216.

49   A. Okur, L. Wickstrom, M. Layten, R. Geney, K. Song, V. Hornak and C. Simmerling, Improved efficiency of replica exchange simulations through use of a hybrid explicit/implicit solvation model, *J. Chem. Theory Comput.*, 2006, **2**, 420–433.

50   R. Geney, M. Layten, R. Gomperts, V. Hornak and C. Simmerling, Investigation of salt bridge stability in a generalized born solvent model, *J. Chem. Theory Comput.*, 2006, **2**, 115–127.

51   M. K. Robinson, J. I. Monroe and M. S. Shell, Are AMBER Force Fields and Implicit Solvation Models Additive? A Folding Study with a Balanced Peptide Test Set, *J. Chem. Theory Comput.*, 2016, **12**, 5631–5642.

52   V. A. Voelz, K. A. Dill and I. Chorny, Peptoid conformational free energy landscapes from implicit-solvent molecular simulations in AMBER., *Biopolymers*, 2011, **96**, 639–650.

53   V. Babin, C. Roland, T. A. Darden and C. Sagui, The free energy landscape of small peptides as obtained from metadynamics with umbrella sampling corrections, *J. Chem. Phys.*, , DOI:10.1063/1.2393236.

54   M. Bonomi, C. Camilloni and M. Vendruscolo, Metadynamic metainference: Enhanced sampling of the metainference ensemble using metadynamics, *Sci. Rep.*, 2016, **6**, 1–11.

55   J. Zhu, Y. Li, J. Wang, Z. Yu, Y. Liu, Y. Tong and W. Han, Adaptive Steered Molecular Dynamics Combined With Protein Structure Networks Revealing the Mechanism of Y68I/G109P Mutations That Enhance the Catalytic Activity of D-psicose 3-Epimerase From Clostridium Bolteae, *Front. Chem.*, , DOI:10.3389/fchem.2018.00437.

56   H. Ndlovu, A. E. Ashcroft, S. E. Radford and S. A. Harris, Effect of sequence variation on the mechanical response of amyloid fibrils probed by steered molecular dynamics simulation, *Biophys. J.*, 2012, **102**, 587–596.

57   Y. Miao, W. Sinko, L. Pierce, D. Bucher, R. C. Walker and J. A. McCammon, Improved reweighting of accelerated molecular dynamics simulations for free energy calculation, *J. Chem. Theory Comput.*, 2014, **10**, 2677–2689.

58   F. Jensen, *Introduction to computational chemistry*, Chichester, UK Hoboken, NJ : John Wiley & Sons, Third edit., 2017.

59   D. A. Case, R. M. Betz, D. S. Cerutti, T. E. Cheatham, T. A. Darden, R. E. Duke, T. J. Giese, H. Gohlke, A. W. Goetz, N. Homeyer, S. Izadi, P. Janowski, J. Kaus, A. Kovalenko, T. S. Lee, S. LeGrand, P. Li, C. Lin, T. Luchko, R. Luo, B. Madej, D. Mermelstein, K. M. Merz, G. Monard, H. Nguyen, H. T. Nguyen, I. Omelyan, A. Onufriev, D. R. Roe, A. Roitberg, C. Sagui, C. L. Simmerling, W. M. Botello-Smith, J. Swails, R. C. Walker, J. Wang, R. M. Wolf, X. Wu, L. Xiao and P. A. Kollman, *AMBER 2016*, San Francisco, 2016.

60   P. Li and K. M. Merz, MCPB.py: A Python Based Metal Center Parameter Builder, *J. Chem. Inf. Model.*, 2016, **56**, 599–604.

61   A. P. Scott and L. Radom, Harmonic vibrational frequencies: An evaluation of Hartree-Fock, Møller-Plesset, quadratic configuration interaction, density functional theory, and semiempirical scale factors, *J. Phys. Chem.*, 1996, **100**, 16502–16513.

62   M. J. Frisch, G. W. Trucks, H. B. Schlegel, G. E. Scuseria, M. A. Robb, J. R. Cheeseman, G. Scalmani, V. Barone, B. Mennucci, G. A. Petersson, H. Nakatsuji, M. Caricato, X. Li, H. P. Hratchian, A. F. Izmaylov, J. Bloino, G. Zheng, J. L. Sonnenberg, M. Hada, M. Ehara, K. Toyota, R. Fukuda, J. Hasegawa, M. Ishida, T. Nakajima, Y. Honda, O. Kitao, H. Nakai, T. Vreven, J. A. Montgomery Jr., J. E. Peralta, F. Ogliaro, M. Bearpark, J. J. Heyd, E. Brothers, K. N. Kudin, V. N. Staroverov, R. Kobayashi, J. Normand, K. Raghavachari, A. Rendell, J. C. Burant, S. S. Iyengar, J. Tomasi, M. Cossi, N. Rega, J. M. Millam, M. Klene, J. E. Knox, J. B. Cross, V. Bakken, C. Adamo, J. Jaramillo, R. Gomperts, R. E. Stratmann, O. Yazyev, A. J. Austin, R. Cammi, C. Pomelli, J. W. Ochterski, R. L. Martin, K. Morokuma, V. G. Zakrzewski, G. A. Voth, P. Salvador, J. J. Dannenberg, S. Dapprich, A. D. Daniels, Ö. Farkas, J. B. Foresman, J. V. Ortiz, J. Cioslowski and D. J. Fox, *Gaussian 09*, Wallingford, CT, 2009.

63   J. M. Seminario, Calculation of intramolecular force fields from second-derivative tensors, *Int. J. Quantum Chem.*, 1996, **60**, 1271–1277.

64   C. I. Bayly, P. Cieplak, W. D. Cornell and P. A. Kollman, A well-behaved electrostatic potential based method using charge restraints for deriving atomic charges: The RESP model, *J. Phys. Chem.*, 1993, **97**, 10269–10280.

65   B. H. Besler, K. M. Merz and P. A. Kollman, Atomic charges derived from semiempirical

methods, *J. Comput. Chem.*, 1990, **11**, 431–439.

66   P. Cieplak, W. D. Cornell, C. Bayly and P. A. Kollman, Application of the multimolecule and multiconformational RESP methodology to biopolymers: Charge derivation for DNA, RNA, and proteins, *J. Comput. Chem.*, 1995, **16**, 1357–1377.

67   K. Lindorff-Larsen, S. Piana, K. Palmo, P. Maragakis, J. L. Klepeis, R. O. Dror and D. E. Shaw, Improved side-chain torsion potentials for the Amber ff99SB protein force field, *Proteins Struct. Funct. Bioinforma.*, 2010, **78**, 1950–1958.

68   J. A. Maier, C. Martinez, K. Kasavajhala, L. Wickstrom, K. E. Hauser and C. Simmerling, ff14SB: Improving the Accuracy of Protein Side Chain and Backbone Parameters from ff99SB, *J. Chem. Theory Comput.*, 2015, **11**, 3696–3713.

69   L. P. Wang, K. A. McKiernan, J. Gomes, K. A. Beauchamp, T. Head-Gordon, J. E. Rice, W. C. Swope, T. J. Martínez and V. S. Pande, Building a More Predictive Protein Force Field: A Systematic and Reproducible Route to AMBER-FB15, *J. Phys. Chem. B*, 2017, **121**, 4023–4039.

70   D. A. Case, I. Y. Ben-Shalom, S. R. Brozell, D. S. Cerutti, I. T.E. Cheatham, V. W. D. Cruzeiro, T. A. Darden, R. E. Duke, D. Ghoreishi, G. Giambasu, T. Giese, M. K. Gilson, H. Gohlke, A. W. Goetz, D. Greene, R. Harris, N. Homeyer, Y. Huang, S. Izadi, A. Kovalenko, R. Krasny, T. Kurtzman, T. S. Lee, S. LeGrand, P. Li, C. Lin, J. Liu, T. Luchko, R. Luo, V. Man, D. J. Mermelstein, K. M. Merz, Y. Miao, G. Monard, C. Nguyen, H. Nguyen, A. Onufriev, F. Pan, R. Qi, D. R. Roe, A. Roitberg, C. Sagui, S. Schott-Verdugo, J. Shen, C. L. Simmerling, J. Smith, J. Swails, R. C. Walker, J. Wang, H. Wei, L. Wilson, R. M. Wolf, X. Wu, L. Xiao, Y. Xiong, D. M. York and P. A. Kollman, *AMBER 2019*, San Francisco, 2019.

71   W. L. Jorgensen, Transferable Intermolecular Potential Functions for Water, Alcohols, and Ethers. Application to Liquid Water, *J. Am. Chem. Soc.*, 1981, **103**, 335–340.

72   W. L. Jorgensen, J. Chandrasekhar, J. D. Madura, R. W. Impey and M. L. Klein, Comparison of simple potential functions for simulating liquid water, *J. Chem. Phys.*, 1983, **79**, 926–935.

73   L. P. Wang, T. J. Martinez and V. S. Pande, Building force fields: An automatic, systematic, and reproducible approach, *J. Phys. Chem. Lett.*, 2014, **5**, 1885–1891.

74   G. D. Hawkins, C. J. Cramer and D. G. Truhlar, *Chem. Phys. Lett.*, 1995, 246, 122–129.

75   G. D. Hawkins, C. J. Cramer and D. G. Truhlar, Parametrized Models of Aqueous Free Energies of Solvation Based on Pairwise Descreening of Solute Atomic Charges from a Dielectric Medium, *J. Phys. Chem.*, 1996, **100**, 19824–19839.

76   H. Nguyen, D. R. Roe and C. Simmerling, Improved generalized born solvent model parameters for protein simulations, *J. Chem. Theory Comput.*, 2013, **9**, 2020–2034.

77   D. R. Roe and T. E. Cheatham, PTRAJ and CPPTRAJ: Software for Processing and Analysis of Molecular Dynamics Trajectory Data, *J. Chem. Theory Comput.*, 2013, **9**, 3084–3095.

78   R. J. Deeth, N. Fey and B. Williams–Hubbard, DommiMOE: An implementation of ligand field molecular mechanics in the molecular operating environment, *J. Comput. Chem.*, 2005, **26**, 123–130.

79   F. Bousejra-ElGarah, C. Bijani, Y. Coppel, P. Faller and C. Hureau, Iron(II) Binding to Amyloid-β, the Alzheimer's Peptide, *Inorg. Chem.*, 2011, **50**, 9024–9030.

80   V. A. Streltsov, S. J. Titmuss, V. C. Epa, K. J. Barnham, C. L. Masters and J. N. Varghese, The structure of the amyloid-beta peptide high-affinity copper II binding site in Alzheimer disease, *Biophys. J.*, 2008, **95**, 3447–3456.

81   R. J. Deeth, The ligand field molecular mechanics model and the stereoelectronic effects of d and s electrons, *Coord. Chem. Rev.*, 2001, **212**, 11–34.

82   J. A. Izaguirre, D. P. Catarello, J. M. Wozniak and R. D. Skeel, Langevin stabilization of molecular dynamics, *J. Chem. Phys.*, 2001, **114**, 2090–2098.

83   J.-P. Ryckaert, G. Ciccotti and H. J. . Berendsen, Numerical integration of the cartesian equations of motion of a system with constraints: molecular dynamics of n-alkanes, *J. Comput. Phys.*, 1977, **23**, 327–341.

84   S. Furlan and G. La Penna, Modeling of the Zn2+ binding in the 1-16 region of the amyloid β peptide involved in Alzheimer's disease, *Phys. Chem. Chem. Phys.*, 2009, **11**, 6468–6481.

85   B. Alies, A. Conte-Daban, S. Sayen, F. Collin, I. Kieffer, E. Guillon, P. Faller and C. Hureau, Zinc(II) Binding Site to the Amyloid-β Peptide: Insights from Spectroscopic Studies with a Wide Series of Modified Peptides, *Inorg. Chem.*, 2016, **55**, 10499–10509.

86   C. M. Kok and A. Rudin, Relationship between the hydrodynamic radius and the radius of gyration of a polymer in solution, *Die Makromol. Chemie, Rapid Commun.*, 1981, **2**, 655–659.

87   J. Danielsson, J. Jarvet, P. Damberg and A. Gräslund, Translational diffusion measured by PFG-NMR on full length and fragments of the Alzheimer Aβ(1-40) peptide. Determination of hydrodynamic radii of random coil peptides of varying length, *Magn. Reson. Chem.*, 2002, **40**, 89–97.

88   C. Talmard, L. Guilloreau, Y. Coppel, H. Mazarguil and P. Faller, Amyloid-Beta Peptide Forms Monomeric Complexes With CuII and ZnII Prior to Aggregation, *ChemBioChem*, 2007, **8**, 163–165.